Published in final edited form as:
J Geophys Res Atmos. 2016 April 27; 121(8): 4296–4316. doi:10.1002/2015jd024343.

Simulating the Black Saturday 2009 smoke plume with an interactive composition-climate model: sensitivity to emissions amount, timing and injection height

Robert D. Field[1,2], **Ming Luo**[3], **Mike Fromm**[4], **Apostolos Voulgarakis**[5], **Stéphane Mangeon**[5], **John Worden**[3]

[1]NASA Goddard Institute for Space Studies, New York, NY, USA

[2]Dept. of Applied Physics and Applied Mathematics, Columbia University, New York, NY, USA

[3]Jet Propulsion Laboratory/California Institute of Technology, Pasadena, CA, USA

[4]Naval Research Laboratory, Washington DC, USA

[5]Department of Physics, Imperial College London, London, UK

Abstract

We simulated the high-altitude smoke plume from the early February 2009 Black Saturday bushfires in southeastern Australia using the NASA GISS ModelE2. To the best of our knowledge, this is the first single-plume analysis of biomass burning emissions injected directly into the upper-troposphere/lower stratosphere (UTLS) using a full-complexity composition-climate model. We compared simulated carbon monoxide (CO) to a new Aura TES/MLS joint CO retrieval, focusing on the plume's initial transport eastward, anticyclonic circulation to the north of New Zealand, westward transport in the lower stratospheric easterlies, and arrival over Africa at the end of February. Our goal was to determine the sensitivity of the simulated plume to prescribed injection height, emissions amount and emissions timing from different sources for a full complexity model when compared to Aura. The most realistic plumes were obtained using injection heights in the UTLS, including one drawn from ground-based radar data. A six-hour emissions pulse or emissions tied to independent estimates of hourly fire behavior produced a more realistic plume in the lower stratosphere compared to the same emissions amount being released evenly over 12 or 24-hours. Simulated CO in the plume was highly sensitive to the differences between emissions amounts estimated from the Global Fire Emissions Database and from detailed, ground-based estimates of fire growth. The emissions amount determined not only the CO concentration of the plume, but the proportion of the plume that entered the stratosphere. We speculate that this is due to either or both non-linear CO loss with a weakened OH sink, or plume self-lofting driven by shortwave absorption of the co-emitted aerosols.

Corresponding author: Robert Field (robert.field@columbia.edu).

1. Introduction

Gases and aerosols are emitted in large quantities from biomass burning, with the dominant constituents being carbon dioxide (CO_2), carbon monoxide (CO), nitrogen oxides (NO_x), volatile organic compounds (VOCs), black carbon, and organic carbon [Andreae and Merlet, 2001]. Global chemical transport models (CTMs) and composition-climate models (CCMs) have been used to investigate global effects of such emissions, which can be large both from an atmospheric chemistry [Mao et al., 2013] and from a climate [Ward et al., 2012] point of view. Studying the effects of biomass burning on the large-scale spatial and temporal variability of atmospheric composition has been done with both types of models [Voulgarakis et al., 2015; Voulgarakis et al., 2010].

Pyroconvective plumes from large fires represent the extreme case of perturbations to atmospheric composition from biomass burning [Fromm et al., 2010]. Uniquely large emissions pulses can be injected directly into the geostrophic flow and dry air at high altitudes in a matter of hours [Fromm et al., 2010]. As a result, they are usually longer-lived, can be transported thousands of kilometers, and can cross the tropopause into the lower stratosphere. Because the emissions pulses are so abrupt relative to other non-volcanic sources, their evolution and decay can be easily separated from background levels of aerosols and trace gases. This makes them useful natural experiments to study with models. Here, we use a global CCM to investigate one such event and to understand its implications for synoptic-scale atmospheric variability and specifically for upper tropospheric/lower stratospheric (UTLS) composition.

Understanding the fate and effects of these plumes through model simulation begins with accurate emissions scenarios, which is a challenge for the extreme fire behavior associated with pyroconvective events. Fuel consumption and energy output can vary by up to three orders of magnitude within a day, and fire behavior can change suddenly from hour-to-hour [Cruz et al., 2012]. Subdaily scales represent the current limit of satellite-based estimates available for use with global-scale models, for example 3-hourly emissions estimates [Mu et al., 2011] from the Global Fire Emissions Database (GFED) [van der Werf et al., 2010], and the 1-hourly estimates from version 1.2 of the Global Fire Assimilation System [Kaiser et al., 2012]. The degree to which global satellite emissions estimates actually represent extreme fire behavior is not well-known, nor is the effect of this possible error source on smoke plume simulation.

As a first step toward full composition-climate modeling of pyroconvective smoke plumes, we assess this uncertainty in simulating a single smoke plume from the 7 February 2009 Black Saturday bushfires in Victoria, Australia. Our focus is to test how variability in injection height, emissions magnitude, and emissions timing affects model-based interpretation of the plume fate, and in the case of Black Saturday, the mechanism through which the plume arrived in the lower stratosphere.

The fires occurred under extreme fire danger conditions associated with dry conditions and a strong, rapidly evolving synoptic disturbance [Engel et al., 2013; Reeder et al., 2015]. Antecedent to Black Saturday, Victoria was enduring drought conditions that were more

extreme than during the country's two prior most significant fire events—Black Friday 1939 and Ash Wednesday 1983. Dirksen et al. [2009] modeled an extreme pyroconvective event in December 2006 from a southeastern Australia using a passive chemical transport model, accurately capturing the plume's rapid transport around the southern hemisphere.

Smoke from the Black Saturday fires was widely observed from different satellite instruments. The plume was injected into relatively pristine southern hemispheric air, standing out easily from background concentrations until arriving over Africa by the end of February, and as it continued westward for several weeks thereafter. Over Africa, the plume was detected in the stratospheric overworld (altitudes above the 380K isentropic surface) [Holton et al., 1995], standing out from background levels of carbon monoxide (CO), hydrogen cyanide (HCN) and ethanenitrile (CH_3CN) from Aura Microwave Limb Sounder (MLS) [Pumphrey et al., 2011], and aerosol-sensitive radiances from the Odin Optical Spectrograph and Infrared Imaging System (OSIRIS) instrument [Siddaway and Petelina, 2011]. Sembhi et al. [2012] showed evidence of the plume up to 20 km using Michaelson Interfermoeter for Passive Atmospheric Sounding (MIPAS) retrievals of a cloud and aerosol top height and a cloud index to infer stratospheric plume heights within the first week of the plume as it became entrained in an anticyclone north of New Zealand. Young and Paton-Walsh [2010] examined different nitrogen dioxide and formaldehyde aging within the plume. Taken together, these studies provide observational constraints on the stratospheric residence of the Black Saturday plume: from 8–9 February to the beginning of June, a period of over 100 days.

Two interpretations of the plume's evolution have been made with different models. de Laat et al. [2012] interpret a variety of satellite-based aerosol observations using a 1D idealized radiative transfer model [Boers et al., 2010]. Their simulations were initialized with a large (3.5) and invariant aerosol optical depth inferred from visible imagery of the young opaque plume, rather than bottom up estimates. They considered injection heights initialized over various layers between 2 and 11 km, among other sensitivity experiments related to emissions timing and smoke optical properties. They argued that rather than initial injection above 11km, which was concluded for Black Saturday [Cruz et al., 2012; Pumphrey et al., 2011] and has been documented for other extreme fires [Fromm et al., 2010; Guan et al., 2010], high absorbing aerosol loads in the plume caused strong shortwave absorption, plume heating, and consequent diabatic lofting.

Glatthor et al. [2013] simulated the plume's fate into early March 2009 using the GEM-AQ chemical transport model, comparing C_2H_2, HCN and HCOOH tracers with simplified chemistry to MIPAS retrievals. They found that observed C2H2/HCN and HCOOH/HCN enhancement ratios in the young plume exceeded model estimates and published values. However, measured and modeled C2H2 and HCOOH e-folding lifetime, based on an exponential fit to enhancement-ratio time series, was reasonably close, as was the overall transport pattern of the modeled plume through February. As they explain, they required an initial injection height of between 14 and 18km to match MIPAS retrievals because of the absence of the aerosol radiative effects in their model. Both models have advantages, detailed aerosol radiative effects in the case of the de Laat et al. [2012] and well-constrained horizontal transport in the case of Glatthor et al. [2013], but required very different

assumptions about the emissions to achieve reasonable agreement with observations of the plume trace gas and aerosol signatures. Most global-scale atmospheric chemistry models use satellite-based estimates of biomass burning [Kaiser et al., 2012; van der Werf et al., 2010], which is the only practical way of doing so consistently at a global scale. Glatthor et al. [2013] , instead used emissions estimates from operational fire reports, which, when available, provide complementary, and often more detailed, information than the satellite-based estimates [Mangeon et al., 2015].

Our interest is in simulating the plume using the NASA GISS ModelE2 composition-climate model to determine 1) the sensitivity of the plume's fate to the very different emissions scenarios from previous studies, namely Laat et al. [2012] and Glatthor et al. [2013], and, 2) the value of increasingly detailed emissions scenarios when these scenarios are available. This follows model-based studies at seasonal or interannual time scales that have examined the sensitivity of modeled composition to injection heights [Veira et al., 2015], emissions amounts [Zhang et al., 2014], and timing [Marlier et al., 2014]. There are fewer studies of this type for single fire events, but we argue that they offer a unique opportunity to understand the sensitivity of modeled plume transport to the uncertainty in estimates of biomass burning emissions scenarios, particularly for cases such as Black Saturday that can now be well-observed from space with better vertical resolution than in early, observational studies of high-altitude plume injections [Fromm et al., 2010].

Black Saturday was a catastrophic event and was the subject of detailed post-fire reporting [Teague et al., 2010]. For the largest of the Black Saturday fires, Kilmore East, this culminated in the detailed fire behavior and radar-based injection height estimates of Cruz et al. [2012]. Following Mangeon et al. [2015], we wanted to determine whether this type of highly detailed fire behavior information leads to more accurate plume simulation, especially when compared to gridded, satellite-based emissions estimates such as GFED which are now standard in CCMs such as ModelE2. We also consider different injection height scenarios, beginning with those from de Laat et al. [2012] and Glatthor et al. [2013], and a range of possible species-specific emissions factors from Andreae and Merlet [2001]. The different injection heights, emissions amounts, and emissions timing considered therefore provide a measure of uncertainty in plume fate across a plausible range of scenarios. We compare our simulations to a new joint CO retrieval constrained by radiances from the Aura Tropospheric Emission (TES) and Microwave Limb Sounder (MLS) instruments [Luo et al., 2013]. We focus on February 2009, when the plume was most easily distinguishable from background CO levels.

The GISS ModelE2 CCM incorporates the strengths of the models used by de Laat et al. [2012] and Glatthor et al. [2013], which, respectively, are radiatively active aerosols and three-dimensional transport. To the best of our knowledge, this is the first CCM simulation of the evolution and fate of a pyroconvective smoke plume. The advantage of using a CCM is to understand, through radiatively interactive composition, the localized effect of the plume on the model's prognostic fields (such as temperature), which in the case of a CTM are prescribed. Understanding the effects of different emissions scenarios is a pre-requisite to more detailed CCM-based interpretation of the plume's evolution and effects, such as localized heating from shortwave absorption, that will be the focus of future work.

2. Data and model

2.1. Aura CO profiles

The Aura satellite was launched in 2004 to a near-polar orbit, carrying the Tropospheric Emission Spectrometer (TES) making nadir infrared measurements, and the Microwave Limb Sounder (MLS) making limb microwave measurements in the CO absorbing spectral bands [Schoeberl et al., 2006]. The radiance measurements from these two instruments are optimally combined to retrieve atmospheric CO profiles with 67 vertical levels as the new Aura CO product V01 [Luo et al., 2013]. TES is a nadir-looking Fourier transform infrared spectrometer with the maximum CO retrieval information in the lower-mid troposphere [Luo et al., 2007]. In 2009, it operated in a one-day-on followed by one-day-off global survey mode with small nadir footprints separated ~180 km along-track. The MLS instrument looks forward at the limb of the atmosphere along the Aura track while performing vertical scans through the upper troposphere and above [Pumphrey et al., 2011]. The TES-MLS observation pairings and the Aura CO retrieval details are described in Luo et al. [2013], in which the February 9–10, 2009 observations of the Black Saturday plume were used to illustrate the CO profile retrieval characteristics. Comparing the stand-alone CO products from TES and MLS respectively, the jointly retrieved Aura CO profiles consist of measurement information from the two instruments for the entire vertical range and are improved in information content in the upper troposphere to lower stratosphere. Typical averaging kernels for the TES, MLS and combined TES-MLS retrievals are shown in Figure 7 of Luo et al [2013]. The combined TES-MLS retrieval has sensitivity spanning those of the individual instruments, resulting in degree of freedom for signal (DOFS) of 2–4 between the surface and 50hPa. Over the MLS influenced vertical range (200 hPa and above), the limb high vertical resolution is defined by its field of view of 2–3 km. The Aura CO retrievals have been evaluated against in-situ balloon and aircraft measurements (Luo et al., 2013 and 2014). The validations show generally good agreement within the retrieval uncertainty of 20–40%. Preliminary validation of Aura CO against HIPPO and MOZAIC data sets indicate that the Aura CO is 20–30% lower over 300–200hPa compared to the in-situ data [Luo et al., 2014] which should be taken into account for model comparisons.

Figure 1 shows Aura CO for three representative periods during the plume's evolution in February, capturing features seen in previous studies. Like in Pumphrey et al. [2011] and Luo et al. [2013], the plume is apparent on February 9/10 east and north of New Zealand between 681 and 316 hPa. It is north of New Zealand between 100 and 68 hPa. On February 19/20 the plume is strictly in the lower stratosphere at 68 hPa and 46 hPa with no detection of the plume in the troposphere. A segment of the plume was detected during this period in MIPAS upper tropospheric C_2H_2, HCN, and HCOOH retrievals over the southern Pacific Ocean and southern South America [Glatthor et al., 2013]. This plume segment was detected briefly at 100 hPa in the MLS-only retrievals [Pumphrey et al., 2011], but not in the combined Aura retrieval due to the more limited coverage of the TES global survey sampling. On February 27/28 the plume is apparent east of Madagascar in the lower stratosphere. We evaluate our model mainly by how well it captures these observed features and avoids generating false plume features for these three periods.

2.2. NASA GISS ModelE2 composition-climate model

We used the GISS ModelE composition-climate model [Schmidt et al., 2014; Shindell et al., 2013], with a 2.0° latitude by 2.5° longitude horizontal resolution and 40 vertical layers from the surface to 0.1 hPa. In all simulations, horizontal winds are nudged toward MERRA reanalysis fields. The model's chemistry includes 156 chemical reactions among 51 gas species. Tropospheric chemistry includes basic NO_x-HO_x-O_x-CO-CH_4 chemistry as well as PANs and the hydrocarbons isoprene, alkyl nitrates, aldehydes, alkenes, and paraffins. The lumped hydrocarbon family scheme was derived from the Carbon Bond Mechanism-4 (CBM-4) [Gery et al., 1989] and from the more extensive Regional Atmospheric Chemistry Model (RACM) [Stockwell et al., 1997], following [Houweling et al., 1998]. To represent stratospheric chemistry, the model includes chlorine- and bromine-containing compounds, and CFC and N_2O source gases (as well as an "age-of-air" passive tracer). As we use only a single CFC tracer, the ratio of anthropogenic bromine to chlorine is held fixed at year 2000 values, with both released from CFC photolysis in an amount proportional to the total equivalent effective stratospheric chlorine loading in a given year. Photolysis rates are simulated using the Fast-J2 scheme [Bian and Prather, 2002; Wild et al., 2000], which accounts for the effects of modeled overhead ozone, clouds, aerosols and surface reflections. The aerosol scheme includes prognostic simulations of the mass distributions of sulfate, sea-salt, dust and carbonaceous aerosols [Koch et al., 2007; Koch et al., 2006]. Secondary organic aerosol production depends on modeled isoprene and terpenes as oxidized by OH, ozone, and nitrate radicals [Tsigaridis and Kanakidou, 2007].

The model's skill in capturing key tropospheric gaseous constituents (e.g. CO which is studied here) and aerosols has been evaluated and shown to be realistic [Koch et al., 2006; Shindell et al., 2013; Voulgarakis et al., 2011]. Also, the model has been thoroughly evaluated on its ability to capture ozone-CO correlations and slopes (which are metrics that indicate the model's ability to capture ozone-related processes in a variety of environments, including those impacted by biomass burning [Jaffe and Wigder, 2012]), and has shown particularly good skill [Voulgarakis et al., 2011].

Biomass burning emissions were added to the model on February 7, 2009 at 37°S, 146°E, northeast of Melbourne, varying the injection height, emissions amount and hourly timing, all described in the next section. The chemistry was configured as above and with simulated chemical and aerosol tracers interacting with the radiation scheme, including absorption of incoming solar radiation. Black Saturday emissions were added for all of CO, NO_x, SO_2, black carbon (BC) and organic carbon (OC), but our model diagnosis was only for CO corresponding to the joint Aura retrieval.

The species profile from the joint Aura TES and MLS retrieval is the optimal estimate of the true state constrained by a priori knowledge. Proper comparisons between the retrieved Aura CO profile and the model profiles are made by applying retrieval smoothing operators to the model profiles [Luo et al., 2013; Luo et al., 2007]. In this study, the model data are sampled at Aura observation locations and times. The sparseness of these sampled data is mostly determined by the TES observation patterns, due to its on-again, off-again sampling

frequency. For a sampled model profile, the following equation is used to estimate what the satellite observing system would retrieve (**x^**) treating the model profile as the true state:

$$\hat{x} = X_a + A(X_{mod} - X_a)$$

where $\mathbf{X_{mod}}$ is the model profile, $\mathbf{X_a}$ is the a priori profile used in Aura CO retrieval, and **A** is the averaging kernel describing the sensitivity of the retrieved Aura CO volume mixing ratio (VMR) to the true state. $\mathbf{X_a}$ and **A** are provided in the Aura CO product files.

2.3. Emissions scenarios

We developed a range of emissions scenarios capturing those in previous studies and from newer information that has become available for Black Saturday. The uncertainty in our model results therefore reflects that across a plausible range of scenarios, rather than from arbitrary and ill-constrained adjustments to the input parameters. The experiments are listed in Table 1 and are described in the following sections. A control experiment was performed with no Black Saturday emissions. Most emissions scenarios considered were large departures from the ModelE2 default biomass burning emissions approach, which was not designed with extreme fire behavior in mind. In the default, the emissions are injected evenly through the planetary boundary layer (between 500m and 1000m over southeast Australia for ModelE2), the emissions amounts are obtained from the daily GFED3 estimates, and the emissions are distributed evenly through the day, with no subdaily variation. In general, our approach was to start with emissions scenarios drawing from previous studies (namely de Laat et al. [2012] and Glatthor et al. [2013]), for the sake of replicating past work with our model. We then progressed through different emissions scenarios that incorporated newly available information, namely the fire behavior estimates for the Kilmore East fire from Cruz et al. [2012].

2.3.1. Injection heights—We started with injection heights in the lower troposphere corresponding to the de Laat et al. [2012] 2–5km ‘low layer initialization’ (deLaat_3.5). For this scenario, emissions were released over 5 model layers centered at 3.5km, representing a simplified vertical emissions profile. Their ‘high layer initialization’ in the mid-upper troposphere between 5–11 km corresponding to their was represented similarly by an emissions release over 5 levels centered at 8.5km (deLaat_8.5. We also considered the upper tropospheric distribution between 14 and 18km from Glatthor et al. [2013] (Glatt_16.5) with a 5-level profile centered at 16.5km. We obtained radar echo top data for stations at Laverton (37.87°S, 144.75°E) and Yarrowonga (36.03°S, 146.02°E) from the Australian Bureau of Meteorology, similar to that in Cruz et al. [2012]. The injection height for this estimate (Radar_13.5) was a 5-level profile centered at 13.5 km. Prior radar analyses of pyroCb events in Australia [Fromm et al., 2006] and Canada [Rosenfeld et al., 2007] showed how these data are informative both for the fire storm’s internal structure and convective injection height. The primary radar analysis we employ is echo-top altitude. This is a conventional radar product for assessing storm tops, and was employed by Rosenfeld et al. [2007] for the Chisholm pyroCb in Alberta in 2001. Here we use a 5 dBZ threshold for the echo-top calculation. The echo-top value we report is from the centroid of the pixel volume. At its considerably greater distance from the pyrogenic targets, the Yarrawonga returns (compared

to Laverton's) are relatively less sensitive to the scattering-feature cross-section, reducing detectability of the plume top.

2.3.2. Emissions amount—We examined plume characteristics for a wide range of emissions amount estimates, which remain uncertain [Kaiser et al., 2012; van der Werf et al., 2010; Voulgarakis and Field, 2015] and can have a significant effect on modeled atmospheric composition [Zhang et al., 2014]. In total, we conducted seven emissions amount tests across the different combinations of fuel consumption and emissions factors, described as follows. Species-specific total emissions are the product of the fuel consumed in Table 1 and the species-specific emissions factors in Table 2.

Glatthor et al.'s [2013] estimate of 2.8 Tg dry matter fuel consumed on February 7 2009 was our starting point. The estimated emissions represent those from the Kilmore East fire only, the largest of the Black Saturday fires, which came from the 2009 Victorian Bushfires Royal Commission [Teague et al., 2010]. We also used daily GFED estimate of 3.2 Tg [Mu et al., 2011] (GFED_StdEF), which are currently the highest temporal resolution used for ModelE2 [Marlier et al., 2014] and can be considered the ModelE2 default. For input to ModelE2, GFED data spatial resolution is reduced to 2° × 2.5° and will capture additional fires beyond Kilmore East, although due to likely low systematic biases in GFED [Clare Paton-Walsh et al., 2012], the estimate of 3.2 Tg fuel consumed for multiple fires is only slightly greater than for the single Kilmore East fire from Glatthor et al. [2013].

Cruz et al. [2012] made detailed fire behavior, fuel consumption and energy output estimates for the Kilmore East fire, drawing on information from fire-fighting agency reports, witness interviews, aircraft-based infrared line-scans during the fire, satellite imagery after the fire, vegetation maps, and post fire fuel consumption. For each of ten 1-hour burn periods, they estimated the size of the fire, predominant fuel types, fractional fuel load consumed, and the total energy output. We converted the energy output into a fuel consumption using a heat of combustion of 18.7 MJ/kg from Glatthor et al. [2013] to obtain a total fuel consumed of 3.3 Tg dry matter over 81 747 ha (CruzKE_StdEF). The Cruz et al. reconstruction of the Kilmore East fire is among the most detailed single wildfire descriptions we are aware of, but which was done for only one fire. To account for the possible contribution of fires other than Kilmore East to high altitude CO, we used the February 7 size estimates from fire behavior estimates from the other large Black Saturday fires [Gellie et al., unpublished manuscript]. We included three additional fires from these estimates: Murrindindi (65 500 ha), Bunyip (21 170 ha), and Churchill (24 280 ha). These fires were added one-at-a-time, but cumulatively, to the CruzKE_StdEF experiment in experiments CruzKEM_StdEF, CruzKEMB_StdEF, and Cruz_KEMBC_StdEF. A map of the final fire perimeters is provided by the Victoria Country Fire Authority (http://www.cfa.vic.gov.au/about/black-saturday/). It was unlikely that there was substantial smoke near the surface from previous days' burning, given that of the four fires considered, only the Bunyip fire was active prior to February 7th. Furthermore, it is reasonable to assume that strong winds at the surface would have ventilated any lingering smoke prior to the extreme fire behavior on the 7th.

The next largest fire burned 13 860 ha; we made the assumption that this and any smaller fires were not intense enough to inject at high altitudes. The Beechworth-Library Road fire

was large (23 900 ha), but burned later in the evening, which we felt was too late for inclusion with the other fires whose behavior and emissions timing was tied to that of Kilmore East. The Gellie report estimate for Kilmore East was 101 300 ha, compared to 81 747 ha across all hourly burn periods by Cruz et al. [2012]. For greater consistency, we scaled the Cruz et al. estimate up by the fraction of the additional fire sizes reported from Gellie relative to their Kilmore East estimate (which effectively reduced sizes of the Gellie estimates). The fuel consumption estimate based on all four fires was 6.8 Tg of dry matter. The exclusion of the Beechworth fire and the downward adjustment of the Gellie fire sizes could make the 6.8 Tg estimate conservative, but, on the other hand, a portion of the smoke emissions from each individual fires was likely released below the prescribed injection heights. We assumed that these factors cancelled each other out and kept 6.8 Tg as the upper end of our fuel consumption estimates.

The uncertainty in species-specific emissions factors should also be considered [van der Werf et al., 2010] alongside uncertainty in fire size and fuel consumed. We did this by varying the emissions factors within the uncertainty ranges provided by Andreae and Merlet [2001]. Emissions factor ranges for each of CO, NO_x, BC and OC are listed in Table 2. No emissions factor ranges were available for SO_2. For all species simultaneously, we applied the low-end emissions factors to the Glatthor fuel consumption scenario (Glatt_LowEF) and the high-end emissions factors to the Cruz/Gellie ‘all-fire’ scenario (CruzKEMBC_HighEF). These two experiments were the end-members for the emissions amounts. Paton-Walsh et al. [2014] recently estimated a CO emissions factor of 120 g kg^{-1} for Australian temperature forest fuel types and Smith et al. [2014] estimated a CO emissions factor of 87 g kg^{-1} for Australian tropical savannas. These newer emissions factors fell within the 77 to 137 g kg^{-1} range from Andreae and Merlet [2001] considered here. We note also that mean CO estimates from the Global Fire Assimilation System [Kaiser et al., 2012] over 2003–2012 tend to be lower than GFED over southeastern Australia [Benedictow et al., 2014] and would presumably fall at the low end of our emissions scenarios.

2.3.3. Emissions timing—We also examined the effect of different emissions timing scenarios using the high emissions amount scenario of 6.8 Tg fuel consumed and the high emissions factors scenario (CruzKEMBC_HighEF). Our default timing was Glatthor et al.’s [2013] pollutant release over 6 hours centered on 11 UTC on February 7. We also released pollutants over a 24-hour mean, which reflects the highest temporal resolution currently used for fire emissions in ModelE2. We also distributed the emissions over a 12-hour mean as an intermediate experiment reflecting a simple assumption about more extreme fire behavior occurring only during daytime, a simplification, for example, of the diurnal fire radiative power estimated from geostationary instruments [Andela et al., 2015]. In these cases, all emissions were released at 13.5km. Lastly, we scaled the emissions linearly to the hourly energy output estimates from Cruz et al. [2012] for Kilmore East. In this case, emissions during the low-intensity periods were injected over 5 layers centered at 3.5km, and during the high intensity periods over 5 layers centered at 13.5km corresponding to the radar estimates, and a simple assumption about high altitude injection being associated only with high fire intensity.

Figure 2 shows the different emissions timing scenarios for the highest emissions case. The Glatthor et al. [2013] 6-hr emissions starting at 11 UTC is the baseline. The 24-hour (effectively the ModelE2 default) and 12-hour distributions broaden the 6-hour distributions from Glatthor et al. [2013]. The emissions scenario (CruzHrly) with hourly timing from Cruz et al. [2012] mostly finish before the Glatthor emissions start. The increased emissions at 07 UTC are consistent with a higher echotop height (Figure 6) and are associated with a dramatic increase in energy output and burned area as the wind shifted from northwesterly to southwesterly, causing the fire's 55km north flank to become its front [Cruz et al., 2012]. For the Cruz hourly scenario, the injection height is 3.5 km for the first 3 hours, 13.5 for the next 5 hours and 3.5km for the next two, corresponding to the injection heights in Figure 6 (in contrast to the other scenarios, where the injection height was constant). Each emissions timing scenario Figure 2 has the same total emissions amount.

3. Results

The control run with no Black Saturday emissions shows the background CO from the lower free troposphere to the lower stratosphere (Figure 3) as it varies during February. The color shading shows the raw model CO averaged over each individual period. The small squares show the model fields with Aura sampling and averaging kernel smoothing corresponding to individual, instantaneous retrievals. The CO values in the small squares are what should be compared directly to the Aura CO in Figure 1. The large white boxes show the regions where the vertical structure of the raw and sampled model fields are compared to the Aura CO profiles. ModelE2 CO at higher altitudes is typically 10–20 ppbv lower than Aura, which is likely due to a low bias in the model, rather than a systematic bias in the Aura CO profiles.

The white contours show the geopotential height at each pressure level. Because the model's horizontal winds have been nudged toward MERRA, the geopotential heights provide a reasonable estimate of the actual large-scale circulation. On February 9th and 10th at 100 hPa, there is a pronounced anticyclonic circulation around a region of high pressure northeast of New Zealand, which was important in the plume 'stalling' for over a week, prior to its advection by Feb 19–20 in the lower stratospheric easterlies, which were also responsible for transporting the plume across the Indian Ocean by the end of February.

3.1. Injection height

Figure 4 shows the model CO for the de Laat et al. [2012] scenario with low layer initialization centered on 3.5km. On February 9/10 there is a CO enhancement peaking ~125 ppb directly east of New Zealand at 681 hPa extending weakly to 316 hPa. The plume position corresponds to the westerly flow in the lower troposphere and agrees qualitatively with the Aura CO over that vertical range. There is no plume signature in the UTLS or for subsequent days, however. Results were similar for a plume centered at 1km (not shown), close to that of the ModelE2 default.

Figure 5 shows the model CO for the de Laat et al. [2012] high layer initialization centered on 8.5 km. On February 9/10, there is a strong plume at 316 hPa northeast of New Zealand that has become weakly entrained in the anticyclonic circulation, agreeing reasonably well

with the Aura CO at that height. There is no plume signature above 316 hPa or for subsequent days.

Figure 6 shows an estimate of injection height from cloud echo top heights from radars near Melbourne. From 4 UTC onward, we treat the injection height as being constrained between 10 and 16 km, but are not trying to capture the variability within that range. Figure 7 shows model CO for a 13.5km injection height corresponding to the middle of the radar echo tops in Figure 6. On February 9/10 there is a strong plume at 100 hPa trapped in the pronounced anticyclonic circulation at that level. There is an enhancement at 68 hPa, but it is very weak, especially relative to the Aura CO. The orbital sampling crosses only the edges of the plume. The raw model CO does not capture the observed plume segment northwest of New Zealand between 100 and 68 hPa. On February 19/20, a weak plume over the Coral Sea (~20°S, 155°E) and NE Australia between 100 hPa and 68 hPa corresponds to the plume with greater CO in Aura. On February 27/28, the plume is apparent east of Madagascar at 68 hPa, but not at 46 hPa. Although the plume at this point has too low CO and is at too low an altitude relative to Aura CO, the fact that it has reached the western Indian Ocean nearly three weeks after the initial emissions suggests injection heights in the UTLS are more realistic for our model.

Figure 8 shows model CO for 16.5 km injection height used by Glatthor et al. [2013]. There is a strong February 9/10 plume at 100 and 68 hPa but, like the 13.5km injection, the model does not capture the observed plume segment north of New Zealand in the Aura retrievals. There is also a large, trailing CO enhancement at 68 hPa for which there is no signature in the Aura CO, the MLS-only CO [Pumphrey et al., 2011] or the C_2H_2 CO at 15km from MIPAS [Glatthor et al., 2013]. This segment appears to be an artificial feature of the model for the 16.5km injection height. On February 19/20 there is a strong enhancement over northeast Australia and the Coral Sea at 68 hPa extending weakly to 46 hPa. There are also segments in the central Pacific at 46 hPa and over the southern tip of South America at 68 hPa. No plume was detected at 46 hPa in the MLS-only data, although there was a plume segment over the southern tip of South America, but at 100 hPa (not shown). The appearance of these Pacific plume segments does suggest that the model is at least capable of simulating plume segments that break off, but in this case in the lower stratosphere, they do not match any observed features. On February 27/28 the plume east of Madagascar is apparent at 68 hPa and appears weakly at 46 hPa. The peak CO is less than Aura, but the horizontal extent, like the 13.5 km plume, agrees well with the observations, especially considering the length of time since the plume release.

3.2. Emissions amount

The 13.5 km (Figure 7) and 16.5km (Figure 8) injection height scenarios captured the plume's transport across Indian Ocean, but the CO concentrations were much less than Aura by the end of the month. This could partly be due to the model's lower spatial resolution, with more pronounced values observed by the retrieval compared to coarser and more diffuse CO in the model. But to additionally test the sensitivity of modeled CO to emissions amount, we considered the emissions amounts listed in Table 1. In all cases, we used emissions centered on a 13.5 km injection height, and the timing from Glatthor et al. [2013].

We focused on the vertical structure of the CO plume for February 9/10 northeast of New Zealand, February 19/20 over the Coral Sea and northeast Australia, and February 27/28 east of Madagascar. We isolated the plume from the background by selecting profiles with CO enhancements above a threshold CO determined by the Aura CO (Figure 1) in boxes containing the observed plume, a simplified approach to Pumphrey et al.'s [2011] isolation of the plume. The thresholds for selecting profiles were: CO greater than 100 ppb at 100 hPa on February 9/10, and CO greater than 30 ppb at 68 hPa on February 19/20 and February 27/28.

The resulting CO profiles over the boxes for the emissions scaling tests are shown in Figure 9. Black horizontal lines define layers in the UTLS (150 hPa to 80 hPa) and strictly lower stratosphere (LS) (80 hPa to 40 hPa) over which sensitivity to emissions will be compared directly. For reference, 'GlattKE_StdEF' emissions is the same experiment as in Figure 7. For the raw model CO (top row) atmospheric CO generally increases with emissions amount. On February 9/10 (Figure 9a), all experiments have their peak enhancement near 100 hPa, and the raw model CO enhancement becomes sharper with increasing emissions. CO at 100 hPa exceeds 600 ppb for the 'CruzKEMBC_HighEF' scenario that had the highest emissions, via inclusion of all four large fires and the high emissions factors from Table 2.

On February 19/20, there is a different vertical response to increasing emissions (Figure 9b). Between 80 and 100 hPa, CO increases across the GlattKE_LowEF and KruzKEM_StdEF scenarios with increasing emissions. For the CruzKEMB_StdEF scenario with the next highest emissions, however, CO between 80 and 100 hPa is actually less, and is offset by greater CO above 80 hPa. This shift continues for the CO profile of the CruzKEMBC_StdEF scenario. The shift is most strongly seen in the CO profile for the CruzKEMBC_HighEF scenario where the CO peak is at 70 hPa. Despite an injection height centered at 13.5km, this scenario has a CO peak at ~ 70 hPa, closer to that of the 16.5 km injection height in Figure 8.

By February 27/28, the shape of the CO profiles, and not just their maximum values, remains separated by emissions amount. The lower emissions scenarios decrease monotonically with height above 100 hPa, whereas the four scenarios including additional fires tend toward a peak enhancement at 70 hPa. The profile for the CruzKEMBC_HighEF scenario is the only one to clearly show an enhancement at 46 hPa.

When the Aura sampling and averaging kernel smoothing are applied (Figure 9, bottom row), the UTLS CO response to increasing emissions is still present, but strongly dampened. On February 9/10, the highest emissions scenario is closest to the Aura CO retrieval, but still with peak values ~60 ppb too low, which is partly because so little of the modeled plume is sampled by the Aura orbit. The four lowest emissions scenarios are difficult to distinguish from one another. The effects of the sampling missing the plume is even more so the case on February 19/20. There is better plume sampling on February 27/28, but the separation in vertical structure between the lower and higher emissions scenarios is mostly lost.

The atmospheric CO responded in both magnitude and vertical structure to the emissions amount. To more clearly understand how atmospheric CO responds to emissions in the UTLS, Figure 10 shows the relationship between CO emissions and CO averaged over the UTLS (150–80 hPa) for the three periods, for both raw model CO (points) and after Aura sampling and averaging kernel smoothing (asterisks). Atmospheric CO is plotted as a function of CO emissions, but we note again that all of BC, OC, NO_x and SO_2 vary with increasing fuel consumed and emissions factors. On February 9/10 for the relatively young plume, there is a near-perfect linear relationship between CO emissions and raw model CO in the UTLS (Figure 10a). With Aura sampling and averaging kernel smoothing, the relationship is similarly strong but with a weaker slope, especially for the low emissions scenarios whose UTLS CO response is harder to separate.

On February 19/20, there is no clear relationship between CO emissions and CO in the UTLS. For the three emissions scenarios between 600 and 800 Gg, there is in fact a decrease in UTLS CO as the plume ascends outside of the low end of the analysis range (Figure 9b). This weak relationship is also the case for the model CO fields after Aura sampling and averaging kernel smoothing, possible reasons for which are considered in the Discussion.

On February 27/28, there is a non-linear relationship between CO emissions and UTLS CO (Figure 10c). For CO emissions greater than 500 Gg, there is little enhancement in UTLS CO. Despite the large increase in CO emissions between the CruKEM_StdEF and CruKEMBC_HighEF emissions scenarios, too little of the plume remains in the UTLS for an emissions increase to yield a response.

Figure 11 is similar to Figure 10, but for CO strictly in the LS. On February 9/10 northeast of New Zealand (Figure 11a), there is a non-linear relationship between CO emissions and LS CO (but note that CO concentrations are much less than in the UTLS in Figure 10a). For CO emissions below 500 Gg, the LS CO does not increase with emissions amount. For emissions above 500 Gg, LS CO increases strongly. On February 19/20 (Figure 11b) there is a linear increase in LS CO for emissions below 500 Gg, little change for the next three scenarios with additional fires but the standard emissions factors, and a jump in LS CO for the highest CruzKEMBC_HighEF scenario. For this scenario, the CO absent in the UTLS (Figure 10b) is instead seen in the LS. On February 27/28 east of Madagascar (Figure 11c), there is a positive and slightly non-linear relationship between emissions and LS CO; although the effect is slight, the CruzKEMBC_HighEF LS CO is higher than we would expect if atmospheric CO increased linearly with emissions. When the Aura operator is applied, these relationships are dampened, but still present.

3.3. Emissions timing

Figure 12 shows mean vertical CO profiles on the three representative periods for the emissions timing scenarios. Overall, the Glatthor et al. [2013] 6hrMean and Cruz et al. [2012] CruzHrly timing deliver more CO to higher altitudes, and the 12 and 24-hour mean emissions to lower altitudes. On February 9/10 the 650 ppbv CO peak for the 6hrMean near 100 hPa is sharper and nearly twice as great as for the 24hrMean timing. By February 19/20, the CO profiles for the higher and lower resolution scenarios have different structures, with the 12hrMean and 24hrMean scenarios having ~90 ppbv CO peaks at 90 hPa, compared to

~70 ppbv peaks at 70 hPa for the 6hrMean and CruzHrly scenarios. By the end of February (Figure 12c), these two timing emissions scenarios result in elevated CO at 46 hPa, where the plume was observed, and the 12hrMean and 24hrMean scenarios do not. The 6hrMean CO peak is ~75 ppbv and the CruzHrly CO peak is ~65ppbv, both at 70 hPa. The 24hrMean and 12hrMean peaks are within this CO range, but peaking at 80 hPa and 100hPa, respectively. The effects of Aura sampling and averaging kernel smoothing are similar to the emissions amount scenarios in strongly muting the response of the CO profile to emissions timing (Figure 12, bottom row).

Figure 13 shows CO maps for the CruzHrly scenario. It has the advantage over the 6-hour pulse (Radar_13.5 in Figure 7 and increased emissions versions of those in Figure 9) of capturing both the lower tropospheric (681 hPa) enhancement on February 9/10 and the UTLS enhancements on February 9/10, 19/20 and 27/28. The lower tropospheric enhancement on February 9/10 is too weak relative to Aura CO and does not extend to 316 hPa, but one can imagine refining the Cruz scenario to better capture the enhancement (with more detailed information about the hourly burned area from other fires described by Gellie, for example), and perhaps distributing more of the emissions in the lower troposphere. The segment of the observed plume northwest of New Zealand on February 9/10 is still absent. On February 19/20 there is also a central Pacific plume segment at 100 hPa. This segment is due to the increased emissions relative to Radar_13.5 in Figure 7 rather than the Cruz timing, given that it also appeared in the high ‘CruzKEMBC_HighEF’ scenario (not shown) but with the highest CO at 68.1 hPa rather than 100 hPa in CruzHrly. This feature did not appear in the joint Aura retrieval because of limited TES sampling frequency but was seen in MLS-only CO retrievals [Pumphrey et al., 2011] and in MIPAS [Glatthor et al., 2013]; we interpret it as a real feature of the plume successfully captured by the model using the CruzHrly scenario. On February 27/28, there is a plume segment trailing back from the central Indian Ocean to southwest Australia which appears to be artificial, and was faintly present for the Glatt_16.5 injection height scenario (Figure 8). In the main plume near Madagascar, peak individual CO concentrations for this scenario exceed 130 ppb.

4. Discussion

The plume fate was highly sensitive to injection height. The 3.5km-centered (Figure 4) and 8.5km-centered (Figure 5) injection heights captured the lower and mid-tropospheric plume segments on February 09/10 (Figure 1), but not the plume segments in the UTLS later in the month that were observed independently with multiple satellite instruments. The differences in plume height and position after two days were significantly different for both injection height scenarios, and these differences grew during the following week (not shown), as the 3.5 km plume was mostly advected eastward over the Pacific, decaying quickly in the lower free troposphere, whereas most of the 8.5 km plume was entrained in the anticyclonic circulation north of New Zealand. This is in contrast to de Laat et al. [2012], who found that the smoke layers converged upon the same mid- to upper- tropospheric range after about 5 days, regardless of which of the two initialization height layers was used. To the extent that the CO diagnosis from our model and the aerosol diagnosis from de Laat et al.’s [2012] idealized model can be compared, we conclude that our plume fate was far more sensitive to injection height than in de Laat et al. [2012]. The plume in ModelE2 did not reach the

stratosphere for strictly tropospheric injection heights, but this does not preclude the existence of the solar escalator mechanism proposed by de Laat et al. [2012], which is discussed further below. But, given the robustness of plume observations in the stratosphere in February 2009 across multiple satellite instruments, this does suggest that the degree of diabatic self-lofting they inferred during the plume's first week was model-specific (as is ours).

Model agreement with lower stratospheric observations of the plume was better for injection heights in the UTLS. Both the 13.5 (Figure 7) and 16.5 km (Figure 8) scenarios produced CO plumes in the lower stratosphere over the western Indian Ocean by the end of February, although with reduced concentrations and at a lower altitude than Aura CO. Insufficient upward flux across the tropopause could also contribute to the lower than observed CO, although stratosphere-troposphere exchange in the model is thought to be realistic, in the mean state at least [Shindell et al., 2013]. In the case of the 16.5km injection height, there was an artificial plume segment with very high CO on February 9/10, which suggests that injection this high is unrealistic for our model.

The importance of high altitude injection for Black Saturday is at the extreme end of realistic injection heights seen in other studies. Turquety et al. [2007] showed over North America that emissions release through the depth of the troposphere produced more realistic model CO relative to MOPITT retrievals, although much of the biomass-burning related CO enhancement was still present for emissions release in the boundary layer only. Veira et al. [2015] considered the effects of different injection height methods with ECHAM6, including the prognostic model of Sofiev et al. [2012], and in one experiment estimated the effect of distributing all wildfire emissions from the boundary layer to the tropopause, which led to unrealistically high black carbon concentrations through the depth of the free troposphere. For our simulation of the Black Saturday CO plume, an upper tropospheric injection height scenario (with high emissions) was necessary to achieve agreement with Aura CO (Figure 13). That this scenario was based on an observed estimate of injection height from radar data (Figure 6) reinforces the value of that data. For modeling studies, it is only realistic to use ground based radar for single plume cases studies like this, but these radar data have promise for validating prognostic plume rise [Veira et al., 2015] and space-based estimates of injection height [Martin et al., 2012].

Though not to the degree of injection height, plume fate was also dependent on emissions timing. Emissions released as a 24-hour mean, corresponding to the highest temporal resolution emissions currently implemented in ModelE2 [Marlier et al., 2014] produced a CO on February 27/28 peaking between 150 hPa and 80 hPa, a lower altitude than Aura CO. Emissions with higher temporal resolution were necessary to capture the observed plume at 46 hPa, and changing the timing for a fixed emissions amount had an effect comparable to changing the amount itself. A steady 6-hour pulse resulted in plume fate similar to emissions released timed according to the hourly Kilmore East energy output from Cruz et al. [2012] (Figure 12c). The differences could be due to emissions being released into different air masses, or reflect a non-linear relationship between emissions amount and plume fate. At a minimum, it does suggest that for extreme fire events, synoptic-level, sub-daily time resolution is necessary. This requirement is likely specific to modeling extreme events such

as Black Saturday. Mu et al. [2011] found that compared to monthly mean emissions, daily emissions improved agreement between modeled and observed CO near biomass burning outflow regions at a seasonal scale, but there was little gain in moving to 3-hourly emissions.

We used what, to the best of our knowledge, was the most detailed fire information available in our estimates of emissions amount, examining the possible contribution of single large fires on Black Saturday and possibly higher emissions factors to CO concentrations three weeks after the fire. This approach for individual fires complements emissions studies at annual and interannual scales to understand the effects on modeled composition of biases in satellite-based emissions estimates [Ichoku et al., 2012; Voulgarakis and Field, 2015]. In our case, higher bottom-up emissions tended to improve agreement with the Aura CO . Improved agreement between modeled and observed composition has been seen in previous studies for both emissions increases and decreases. In characterizing simulated South American biomass burning emissions fate and their plume rise model, Archer-Nicholls et al. [2015] incorporated reduced fire sizes to improve their prognostic injection heights (which were prescribed in our simulations), but this required scaling the emissions upward by a factor of 5 to obtain reasonable agreement with aerosol optical depth measurements. Kaiser et al. [2012] and Tosca et al. [2013] required increases in aerosol emissions scaling factors of 3.4 and 1.97, respectively, to obtain reasonable model agreement with AOD globally. By contrast, Parrington et al. [2012] and Fisher et al. [2010] required significant emissions reductions to achieve better agreement with CO retrievals and aircraft measurements in the Arctic troposphere, respectively. In all cases, the a priori estimates were obtained from satellite-based estimates of fire size or radiative power and scaled to improve agreement with observations. We argue that comparing the satellite bottom-up estimates for individual fires to independent estimates such as Cruz et al. [2012] have value in understanding why the satellite bottom-up estimates may be biased, keeping in mind that background model biases in ‘clean’ conditions (as in the control simulation of Figure 3) must be considered to avoid any overcompensation through emissions adjustments.

The emissions amount sensitivity experiments also showed the changing relationship between emissions and atmospheric CO as the plume evolved during February (Figure 10). In ModelE2, the emissions amount determined not only the CO levels of the plume, but the proportion of the plume that entered the stratosphere, to the point where on February 19/20 for the highest CruzKEMBC_HighEF emissions scenario, the UTLS CO decreased and LS CO increased. Two possible reasons for this are:

1. Effects of CO emissions on their own lifetime. Increases of CO will lead to greater consumption of OH, and since oxidation by OH is a major CO sink [Voulgarakis et al., 2015], this could potentially be acting as a positive feedback.
2. Direct UTLS injection with subsequent self-lofting associated with co-varying changes in absorbing aerosol emissions, primarily BC. That is, because the aerosols in the model are radiatively active, increases in BC could lead to more shortwave absorption, plume heating, and diabatic ascent of the CO-containing plume. The CO rises higher into the stratosphere than if no shortwave absorption were taking place concurrently.

Devenish et al. [2009] identified the role of self-lofting for a lower tropospheric smoke plume from a large industrial fire in the UK using large-eddy simulations, but, other than this, we are unaware of other studies with high-complexity models with self-lofting constrained by observations in this way. In their model-only study, Mao et al. [2013] found in the GFDL AM3 that the global CO burden increased linearly with increasing gaseous emissions from biomass burning, but non-linearly when the same scaling was applied to the biomass burning aerosol emissions also. They attributed this non-linearity to the aerosol uptake of OH sources such as HO_2, and a consequent weakening of the primary CO sink by OH. This heterogeneous process is not yet included in ModelE2, so is not a possible factor contributing to a positive feedback in our simulations, but warrants further examination.

The non-linear increase in CO concentrations with emissions amount also needs to be considered alongside other studies where the response of the atmospheric aerosol burden to emissions was damped. Veira et al. [2015] found that a 57% increase in wildfire BC emissions led to only a 39% increase in the global atmospheric BC burden. As they state, similar damping effects in response of BC concentrations to emissions were seen across Africa in Zhang et al. [2014]. In both cases, however, the damped global responses were punctuated by larger local responses dependent on regional transport patterns and fire activity.

5. Conclusions

We have conducted the first full-complexity CCM simulation of a single, high-altitude smoke plume originating from a pyroconvective fire, examining the sensitivity of the plume fate to the prescribed emissions injection height, amount and timing. For ModelE2, injection heights into the UTLS constrained by ground-based radar produced a far more realistic plume simulation than strictly tropospheric injection heights. Agreement with Aura CO improved with increasing emissions, which we based on estimated contributions from individual fires. Hourly and 6-hourly emissions timing captured multiple plume segments better than emissions released evenly over 12 or 24-hours. Our estimates of emissions injection height, emissions amount, and emissions timing were obtained largely from ground-based sources, which we argue are an invaluable but largely overlooked source of data for these types of studies. At minimum, they have considerable untapped potential for evaluating global-scale emissions data sets that are now standard for CCMs and CTMs [Mangeon et al., 2015].

Further work will focus on individual emissions increases, particularly aerosols, and diagnosis of CO loss, which may be necessary to understand what is driving the complicated relationship between emissions and CO concentration in the UTLS. It will also help to understand the persistence of the plume in the lower stratosphere until mid-June seen in the Optical Spectrograph and Infrared Imager System (OSIRIS) [Siddaway and Petelina, 2011] and Cloud-Aerosol Lidar with Orthogonal Polarization (CALIOP) [Vernier et al., 2011].We will also examine the chemical and thermal evolution of such plumes and the climatic effects of multiple plume injections at high altitudes.

Acknowledgements

Laverton and Yarrowonga Radar data were obtained from the Australian Bureau of Meteorology. We thank Nicholas Gellie for the use of his unpublished area burned estimates for the Black Saturday fires. RDF and MF were supported by NASA ROSES Atmospheric Modeling and Analysis Program grant NNX13AK46G. AV and SM were supported by the Natural Environment Research Council and the UK Met Office. Research was partially supported by the Jet Propulsion Laboratory, California Institute of Technology under contract to the National Aeronautics and Space Administration (NASA). Resources supporting this work were provided by the NASA High-End Computing (HEC) Program through the NASA Center for Climate Simulation (NCCS) at Goddard Space Flight Center. All data in the study can be obtained by contacting the lead author.

References

Andela N, Kaiser JW, van der Werf GR, and Wooster MJ (2015), New fire diurnal cycle characterizations to improve fire radiative energy assessments made from MODIS observations, Atmospheric Chemistry and Physics, 15(15), 8831–8846, doi:10.5194/acp-15-8831-2015.

Andreae MO, and Merlet P (2001), Emission of trace gases and aerosols from biomass burning, Global Biogeochemical Cycles, 15(4), 955–966, doi:10.1029/2000gb001382.

Archer-Nicholls S, et al. (2015), Characterising Brazilian biomass burning emissions using WRF-Chem with MOSAIC sectional aerosol, Geoscientific Model Development, 8(3), 549–577, doi:10.5194/gmd-8-549-2015.

Benedictow A, et al. (2014), Validation report of the MACC reanalysis of global atmospheric composition: Period 2003–2012.Rep., 96 pp.

Bian HS, and Prather MJ (2002), Fast-J2: Accurate simulation of stratospheric photolysis in global chemical models, Journal of Atmospheric Chemistry, 41(3), 281–296, doi:10.1023/a:1014980619462.

Boers R, de Laat AT, Zweers DCS, and Dirksen RJ (2010), Lifting potential of solar-heated aerosol layers, Geophysical Research Letters, 37, doi:10.1029/2010gl045171.

Cruz MG, Sullivan AL, Gould JS, Sims NC, Bannister AJ, Hollis JJ, and Hurley RJ (2012), Anatomy of a catastrophic wildfire: The Black Saturday Kilmore East fire in Victoria, Australia, Forest Ecology and Management, 284, 269–285, doi:10.1016/j.foreco.2012.02.035.

de laat ATJ, Zweers DCS, Boers R, and Tuinder ONE (2012), A solar escalator: Observational evidence of the self-lifting of smoke and aerosols by absorption of solar radiation in the February 2009 Australian Black Saturday plume, Journal of Geophysical Research-Atmospheres, 117, doi:10.1029/2011jd017016.

Devenish BJ, and Edwards JM (2009), Large-eddy simulation of the plume generated by the fire at the Buncefield oil depot in December 2005, Proceedings of the Royal Society a-Mathematical Physical and Engineering Sciences, 465(2102), 397–419, doi:10.1098/rspa.2008.0288.

Dirksen RJ, Boersma KF, de Laat J, Stammes P, van der Werf GR, Martin MV, and Kelder HM (2009), An aerosol boomerang: Rapid around-the-world transport of smoke from the December 2006 Australian forest fires observed from space, Journal of Geophysical Research-Atmospheres, 114, doi:10.1029/2009jd012360.

Engel CB, Lane TP, Reeder MJ, and Rezny M (2013), The meteorology of Black Saturday, Quarterly Journal of the Royal Meteorological Society, 139(672), 585–599, doi:10.1002/qj.1986.

Fisher JA, et al. (2010), Source attribution and interannual variability of Arctic pollution in spring constrained by aircraft (ARCTAS, ARCPAC) and satellite (AIRS) observations of carbon monoxide, Atmospheric Chemistry and Physics, 10(3), 977–996.

Fromm M, Lindsey DT, Servranckx R, Yue G, Trickl T, Sica R, Doucet P, and Godin-Beekmann SE (2010), The Untold Story of Pyrocumulonimbus, Bulletin of the American Meteorological Society, 91(9), 1193–1209, doi:10.1175/2010bams3004.1.

Fromm M, Tupper A, Rosenfeld D, Servranckx R, and McRae R (2006), Violent pyroconvective storm devastates Australia's capital and pollutes the stratosphere, Geophysical Research Letters, 33(5), doi:10.1029/2005gl025161.

Gery MW, Whitten GZ, Killus JP, and Dodge MC (1989), A photochemical kinetics mechanism for urban and regional scale computer modeling, Journal of Geophysical Research-Atmospheres, 94(D10), 12925–12956, doi:10.1029/JD094iD10p12925.

Glatthor N, et al. (2013), The Australian bushfires of February 2009: MIPAS observations and GEM-AQ model results, Atmospheric Chemistry and Physics, 13(3), 1637–1658, doi:10.5194/acp-13-1637-2013.

Guan H, Esswein R, Lopez J, Bergstrom R, Warnock A, Follette-Cook M, Fromm M, and Iraci LT (2010), A multi-decadal history of biomass burning plume heights identified using aerosol index measurements, Atmospheric Chemistry and Physics, 10(14), 6461–6469, doi:10.5194/acp-10-6461-2010.

Holton JR, Haynes PH, McIntyre ME, Douglass AR, Rood RB, and Pfister L (1995), Stratosphere-troposphere exchange, Reviews of Geophysics, 33(4), 403–439, doi:10.1029/95rg02097.

Houweling S, Dentener F, and Lelieveld J (1998), The impact of nonmethane hydrocarbon compounds on tropospheric photochemistry, Journal of Geophysical Research-Atmospheres, 103(D9), 10673–10696, doi:10.1029/97jd03582.

Ichoku C, Kahn R, and Chin M (2012), Satellite contributions to the quantitative characterization of biomass burning for climate modeling, Atmospheric Research, 111, 1–28, doi:10.1016/j.atmosres.2012.03.007.

Jaffe DA, and Wigder NL (2012), Ozone production from wildfires: A critical review, Atmospheric Environment, 51, 1–10, doi:10.1016/j.atmosenv.2011.11.063.

Kaiser JW, et al. (2012), Biomass burning emissions estimated with a global fire assimilation system based on observed fire radiative power, Biogeosciences, 9(1), 527–554, doi:10.5194/bg-9-527-2012.

Koch D, Bond TC, Streets D, and Unger N (2007), Linking future aerosol radiative forcing to shifts in source activities, Geophysical Research Letters, 34(5), doi:10.1029/2006gl028360.

Koch D, Schmidt GA, and Field CV (2006), Sulfur, sea salt, and radionuclide aerosols in GISS ModelE, Journal of Geophysical Research-Atmospheres, 111(D6), doi:10.1029/2004jd005550.

Luo M, Read W, Kulawik S, Worden J, Livesey N, Bowman K, and Herman R (2013), Carbon monoxide (CO) vertical profiles derived from joined TES and MLS measurements, Journal of Geophysical Research-Atmospheres, 118(18), 10601–10613, doi:10.1002/jgrd.50800.

Luo M, et al. (2007), Comparison of carbon monoxide measurements by TES and MOPITT: Influence of a priori data and instrument characteristics on nadir atmospheric species retrievals, Journal of Geophysical Research-Atmospheres, 112(D9), doi:10.1029/2006jd007663.

Luo M, Schwartz M, Read W, Herman R, Kulawik S, Worden J, Livesey N, Bowman K, and Sweeney C (2014), Introducing and Validating the New Aura CO Product Derived from Joined TES and MLS measurements, in AGU Fall Meeting, edited, San Francisco, CA.

Mangeon S, Field RD, McHugh C, Fromm M, and Voulgarakis A (2015), A comparison between MODIS-based burned area and fire agency reports over North America in 2007, Anthropocene, accepted.

Mao J, Horowitz LW, Naik V, Fan S, Liu J, and Fiore AM (2013), Sensitivity of tropospheric oxidants to biomass burning emissions: implications for radiative forcing, Geophysical Research Letters, 40(6), 1241–1246, doi:10.1002/grl.50210.

Marlier ME, Voulgarakis A, Shindell DT, Faluvegi G, Henry CL, and Randerson JT (2014), The role of temporal evolution in modeling atmospheric emissions from tropical fires, Atmospheric Environment, 89, 158–168, doi:10.1016/j.atmosenv.2014.02.039.

Martin MV, Kahn RA, Logan JA, Paugam R, Wooster M, and Ichoku C (2012), Space-based observational constraints for 1-D fire smoke plume-rise models, Journal of Geophysical Research-Atmospheres, 117, doi:10.1029/2012jd018370.

Mu M, et al. (2011), Daily and 3-hourly variability in global fire emissions and consequences for atmospheric model predictions of carbon monoxide, Journal of Geophysical Research-Atmospheres, 116, doi:10.1029/2011jd016245.

Parrington M, et al. (2012), The influence of boreal biomass burning emissions on the distribution of tropospheric ozone over North America and the North Atlantic during 2010, Atmospheric Chemistry and Physics, 12(4), 2077–2098, doi:10.5194/acp-12-2077-2012.

Paton-Walsh C, Emmons LK, and Wiedinmyer C (2012), Australia's Black Saturday fires - Comparison of techniques for estimating emissions from vegetation fires, Atmospheric Environment, 60, 262–270, doi:10.1016/j.atmosenv.2012.06.066.

Paton-Walsh C, Smith TEL, Young EL, Griffith DWT, and Guerette EA (2014), New emission factors for Australian vegetation fires measured using open-path Fourier transform infrared spectroscopy - Part 1: Methods and Australian temperate forest fires, Atmospheric Chemistry and Physics, 14(20), 11313–11333, doi:10.5194/acp-14-11313-2014.

Pumphrey HC, Santee ML, Livesey NJ, Schwartz MJ, and Read WG (2011), Microwave Limb Sounder observations of biomass-burning products from the Australian bush fires of February 2009, Atmospheric Chemistry and Physics, 11(13), 6285–6296, doi:10.5194/acp-11-6285-2011.

Reeder MJ, Spengler T, and Musgrave R (2015), Rossby waves, extreme fronts, and wildfires in southeastern Australia, Geophysical Research Letters, 42(6), 2015–2023, doi:10.1002/2015gl063125.

Rosenfeld D, Fromm M, Trentmann J, Luderer G, Andreae MO, and Servranckx R (2007), The Chisholm firestorm: observed microstructure, precipitation and lightning activity of a pyro-cumulonimbus, Atmospheric Chemistry and Physics, 7, 645–659.

Schmidt GA, et al. (2014), Configuration and assessment of the GISS ModelE2 contributions to the CMIP5 archive, Journal of Advances in Modeling Earth Systems, 6(1), 141–184, doi:10.1002/2013ms000265.

Schoeberl MR, et al. (2006), Overview of the EOS Aura Mission, Ieee Transactions on Geoscience and Remote Sensing, 44(5), 1066–1074, doi:10.1109/tgrs.2005.861950.

Sembhi H, Remedios J, Trent T, Moore DP, Spang R, Massie S, and Vernier JP (2012), MIPAS detection of cloud and aerosol particle occurrence in the UTLS with comparison to HIRDLS and CALIOP, Atmospheric Measurement Techniques, 5(10), 2537–2553, doi:10.5194/amt-5-2537-2012.

Shindell DT, et al. (2013), Interactive ozone and methane chemistry in GISS-E2 historical and future climate simulations, Atmospheric Chemistry and Physics, 13(5), 2653–2689, doi:10.5194/acp-13-2653-2013.

Siddaway JM, and Petelina SV (2011), Transport and evolution of the 2009 Australian Black Saturday bushfire smoke in the lower stratosphere observed by OSIRIS on Odin, Journal of Geophysical Research-Atmospheres, 116, doi:10.1029/2010jd015162.

Smith TEL, Paton-Walsh C, Meyer CP, Cook GD, Maier SW, Russell-Smith J, Wooster MJ, and Yates CP (2014), New emission factors for Australian vegetation fires measured using open-path Fourier transform infrared spectroscopy - Part 2: Australian tropical savanna fires, Atmospheric Chemistry and Physics, 14(20), 11335–11352, doi:10.5194/acp-14-11335-2014.

Sofiev M, Ermakova T, and Vankevich R (2012), Evaluation of the smoke-injection height from wild-land fires using remote-sensing data, Atmospheric Chemistry and Physics, 12(4), 1995–2006, doi:10.5194/acp-12-1995-2012.

Stockwell WR, Kirchner F, Kuhn M, and Seefeld S (1997), A new mechanism for regional atmospheric chemistry modeling, Journal of Geophysical Research-Atmospheres, 102(D22), 25847–25879, doi:10.1029/97jd00849.

Teague B, McLeoad D, and Pascoe S (2010), 2009 Victorian Bushfires Royal Commission Final Report*Rep*.

Tosca MG, Randerson JT, and Zender CS (2013), Global impact of smoke aerosols from landscape fires on climate and the Hadley circulation, Atmospheric Chemistry and Physics, 13(10), 5227–5241, doi:10.5194/acp-13-5227-2013.

Tsigaridis K, and Kanakidou M (2007), Secondary organic aerosol importance in the future atmosphere, Atmospheric Environment, 41(22), 4682–4692, doi:10.1016/j.atmosenv.2007.03.045.

Turquety S, et al. (2007), Inventory of boreal fire emissions for North America in 2004: Importance of peat burning and pyroconvective injection, Journal of Geophysical Research-Atmospheres, 112(D12), doi:10.1029/2006jd007281.

van der Werf GR, Randerson JT, Giglio L, Collatz GJ, Mu M, Kasibhatla PS, Morton DC, DeFries RS, Jin Y, and van Leeuwen TT (2010), Global fire emissions and the contribution of deforestation,

savanna, forest, agricultural, and peat fires (1997–2009), Atmospheric Chemistry and Physics, 10(23), 11707–11735, doi:10.5194/acp-10-11707-2010.

Veira A, Kloster S, Schutgens NAJ, and Kaiser JW (2015), Fire emission heights in the climate system - Part 2: Impact on transport, black carbon concentrations and radiation, Atmospheric Chemistry and Physics, 15(13), 7173–7193, doi:10.5194/acp-15-7173-2015.

Vernier JP, Pommereau JP, Thomason LW, Pelon J, Garnier A, Deshler T, Jumelet J, and Nielsen JK (2011), Overshooting of clean tropospheric air in the tropical lower stratosphere as seen by the CALIPSO lidar, Atmospheric Chemistry and Physics, 11(18), 9683–9696, doi:10.5194/acp-11-9683-2011.

Voulgarakis A, and Field RD (2015), Fire influences on atmospheric composition, air quality, and climate, Current Pollution Reports, doi:10.1007/s40726-015-0007-z.

Voulgarakis A, Marlier ME, Faluvegi G, Shindell DT, Tsigaridis K, and Mangeon S (2015), Interannual variability of tropospheric trace gases and aerosols: The role of biomass burning emissions, Journal of Geophysical Research - Atmospheres, 120, doi:10.1002/2014JD022926.

Voulgarakis A, Savage NH, Wild O, Braesicke P, Young PJ, Carver GD, and Pyle JA (2010), Interannual variability of tropospheric composition: the influence of changes in emissions, meteorology and clouds, Atmospheric Chemistry and Physics, 10(5), 2491–2506, doi:10.5194/acp-10-2491-2010.

Voulgarakis A, Telford PJ, Aghedo AM, Braesicke P, Faluvegi G, Abraham NL, Bowman KW, Pyle JA, and Shindell DT (2011), Global multi-year O-3-CO correlation patterns from models and TES satellite observations, Atmospheric Chemistry and Physics, 11(12), 5819–5838, doi:10.5194/acp-11-5819-2011.

Ward DS, Kloster S, Mahowald NM, Rogers BM, Randerson JT, and Hess PG (2012), The changing radiative forcing of fires: global model estimates for past, present and future, Atmospheric Chemistry and Physics, 12(22), 10857–10886, doi:10.5194/acp-12-10857-2012.

Wild O, Zhu X, and Prather MJ (2000), Fast-j: Accurate simulation of in- and below-cloud photolysis in tropospheric chemical models, Journal of Atmospheric Chemistry, 37(3), 245–282, doi:10.1023/a:1006415919030.

Young EL, Paton-Walsh C, and Iop (2010), Formaldehyde and nitrogen dioxide in smoke plumes from Australia's Black Saturday fires, 17th National Conference of the Australian Meteorological and Oceanographic Society, 11, doi:10.1088/1755-1315/11/1/012023.

Zhang F, et al. (2014), Sensitivity of mesoscale modeling of smoke direct radiative effect to the emission inventory: a case study in northern sub-Saharan African region, Environmental Research Letters, 9(7), doi:10.1088/1748-9326/9/7/075002.

Key points

- stratospheric plume fate was highly sensitive to emissions height, amount and timing
- there were non-linear relationships between emissions and atmospheric CO in the UTLS
- a possible reason is diabatic self-lofting of the plume through shortwave absorption

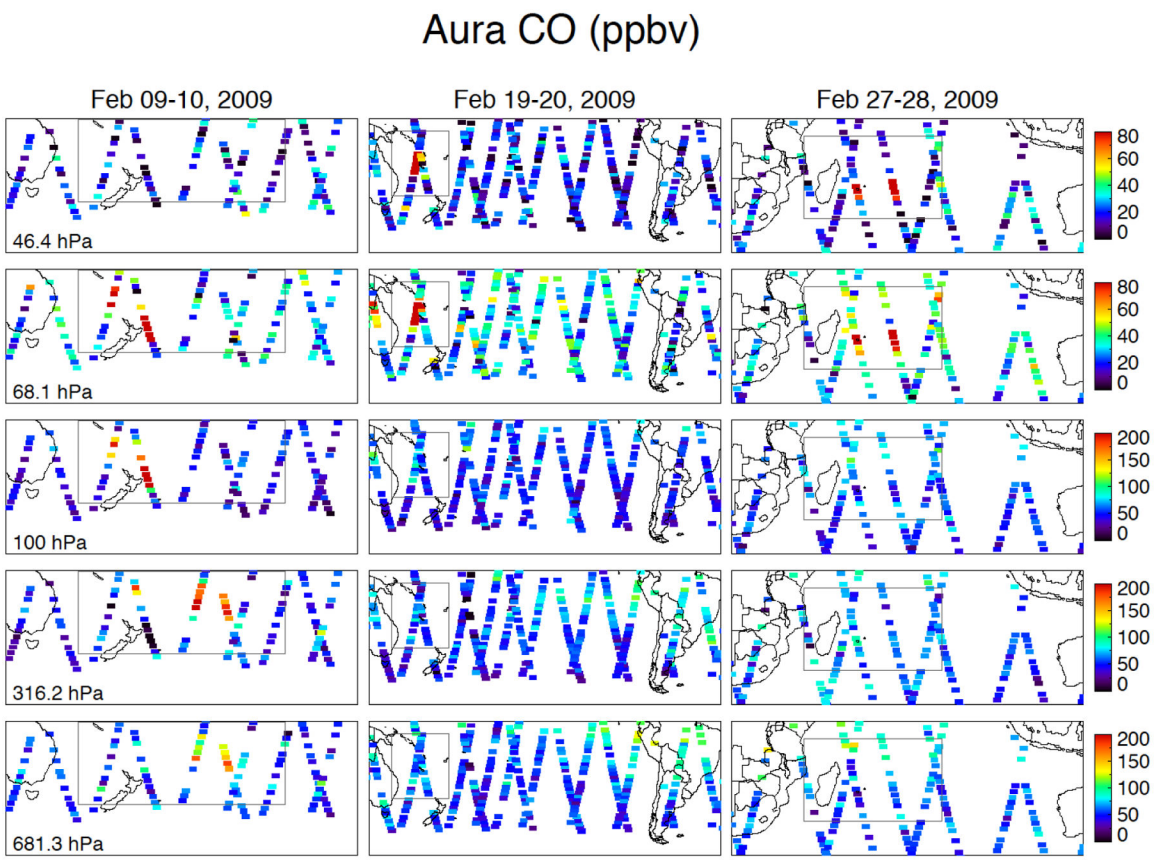

Figure 1.

Aura CO between 681 hPa and 46 hPa for three representative days in February showing the plume's ascent into the lower stratosphere. Thin rectangles show the regions over which the vertical structure of the CO was examined.

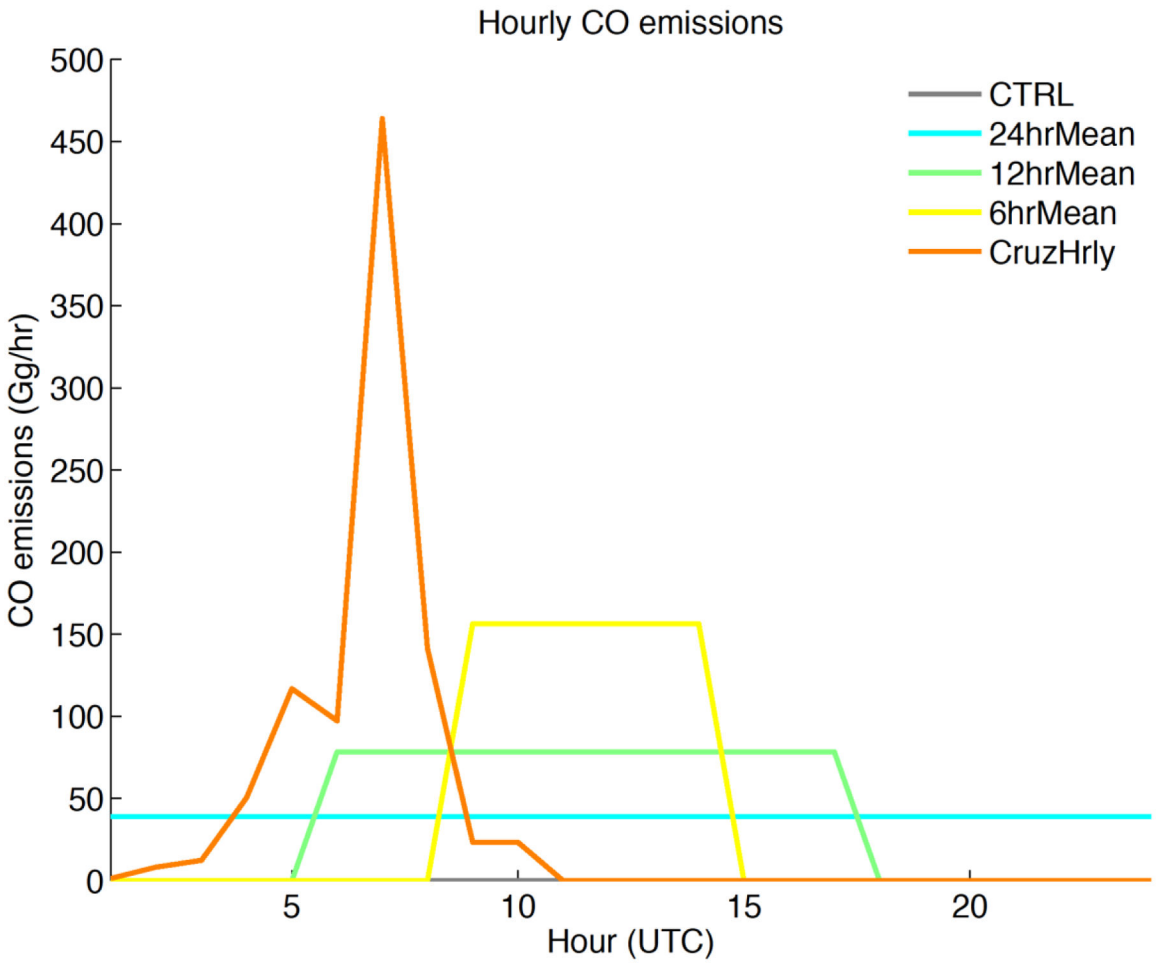

Figure 2.
Different emissions timing scenarios (see Table 1) for the high emissions amount (CruzKEMBC_HighEF) case.

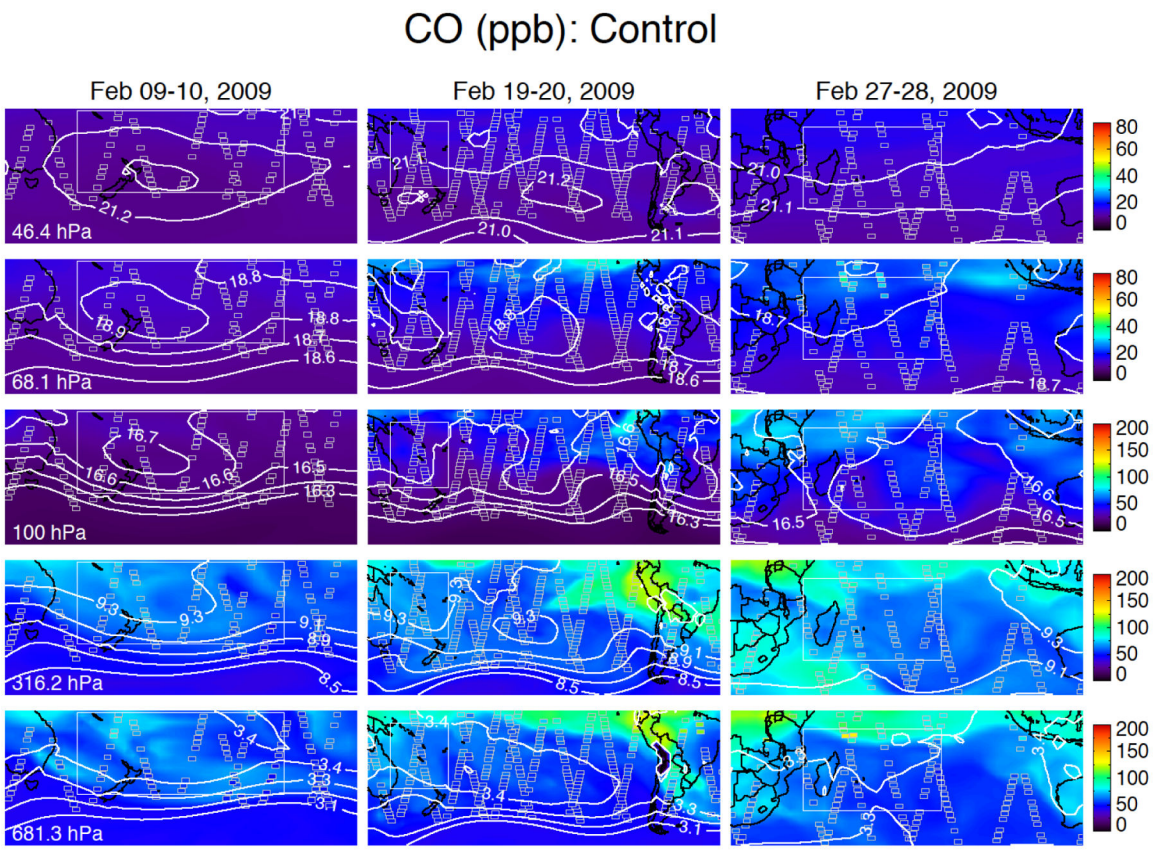

Figure 3.

ModelE2 control run (CTRL) with no fire. Colored shading shows raw ModelE2 CO (ppb) (note changes in CO scale with height). Small boxes show the ModelE2 CO (ppb) sampled along the Aura orbit and with averaging kernel smoothing. White contours show geopotential height in km. Large white boxes show boxes over which CO profiles are averaged.

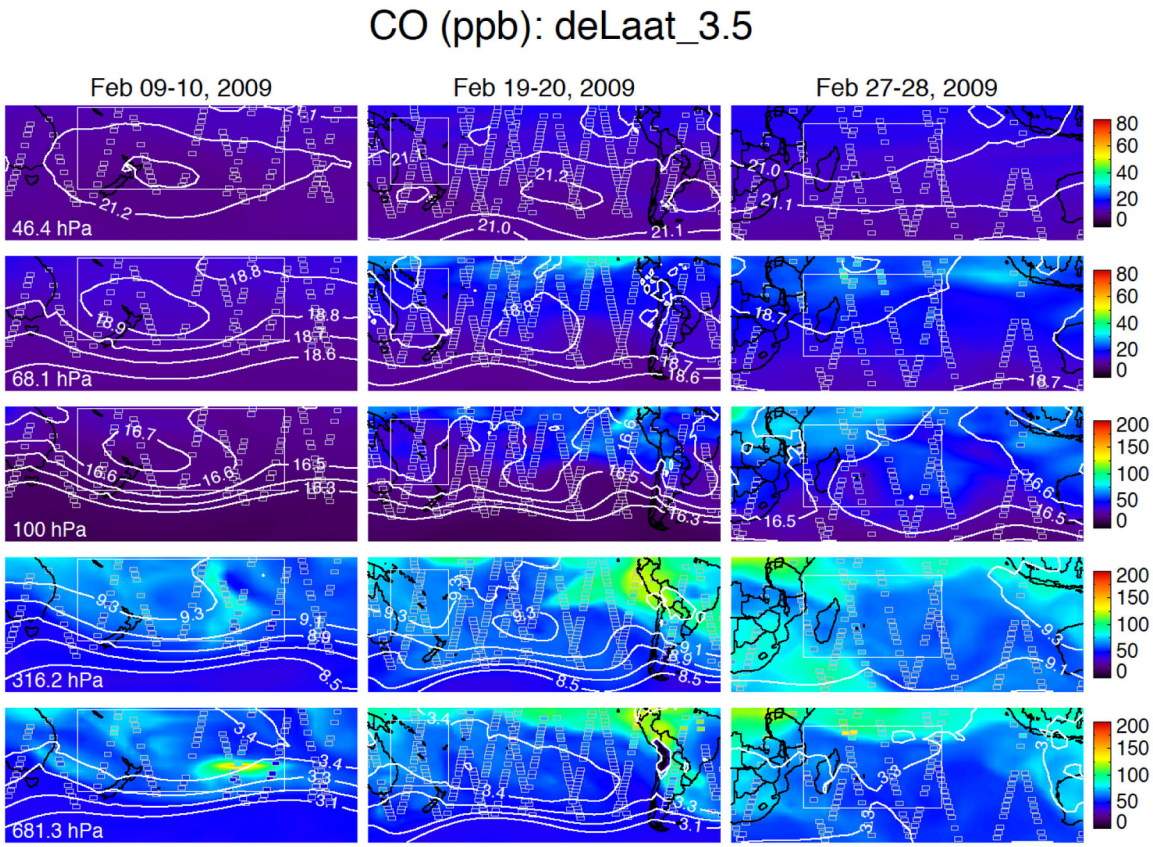

Figure 4.

de Laat et al. [2012] 3.5 km injection height with Glatthor et al. [2013] fuel consumption of 2.8 Tg for 6 hours starting at 11:00 UTC on February 7. Colored shading shows raw ModelE2 CO (ppb) (note changes in CO scale with height). Small boxes show the ModelE2 CO (ppb) sampled along the Aura orbit and with averaging kernel smoothing. White contours show geopotential height in km. Large white boxes show boxes over which CO profiles are averaged.

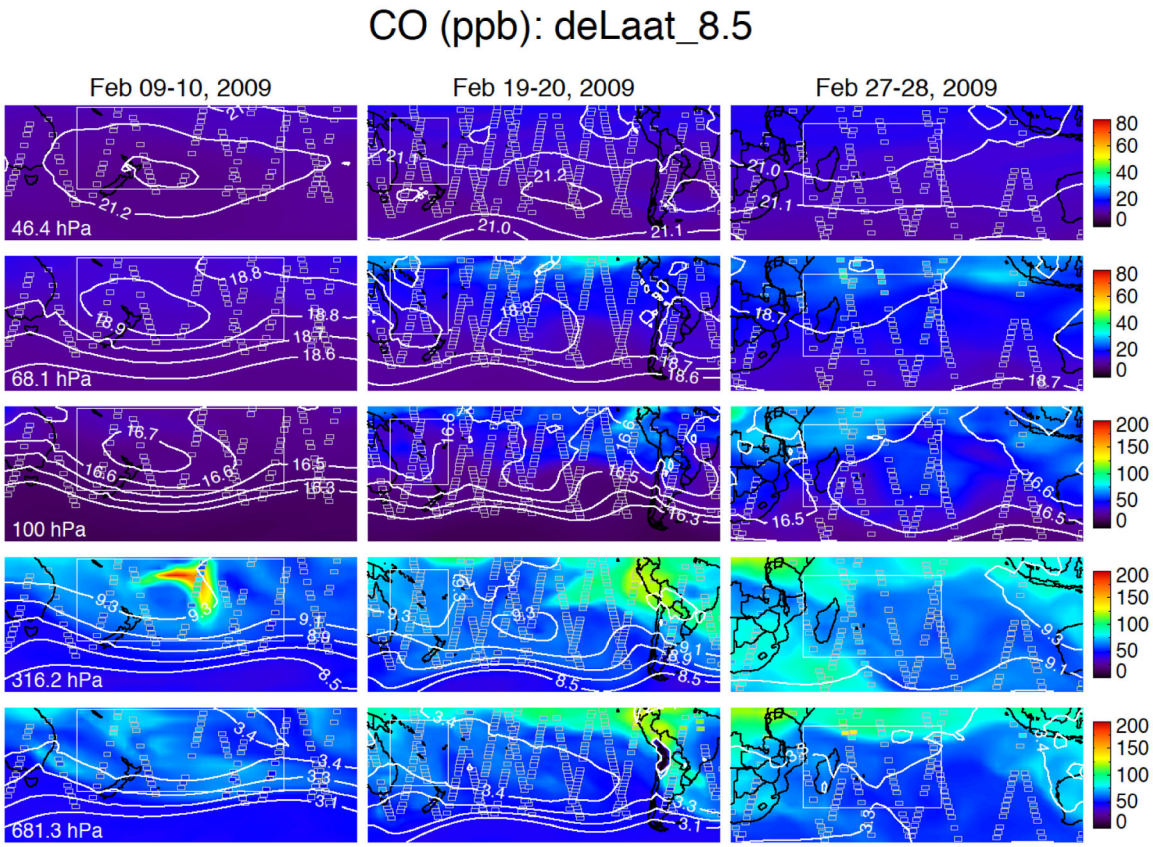

Figure 5.
Same as Figure 4, but for the de Laat et al. [2012] 8.5 km injection height scenario.

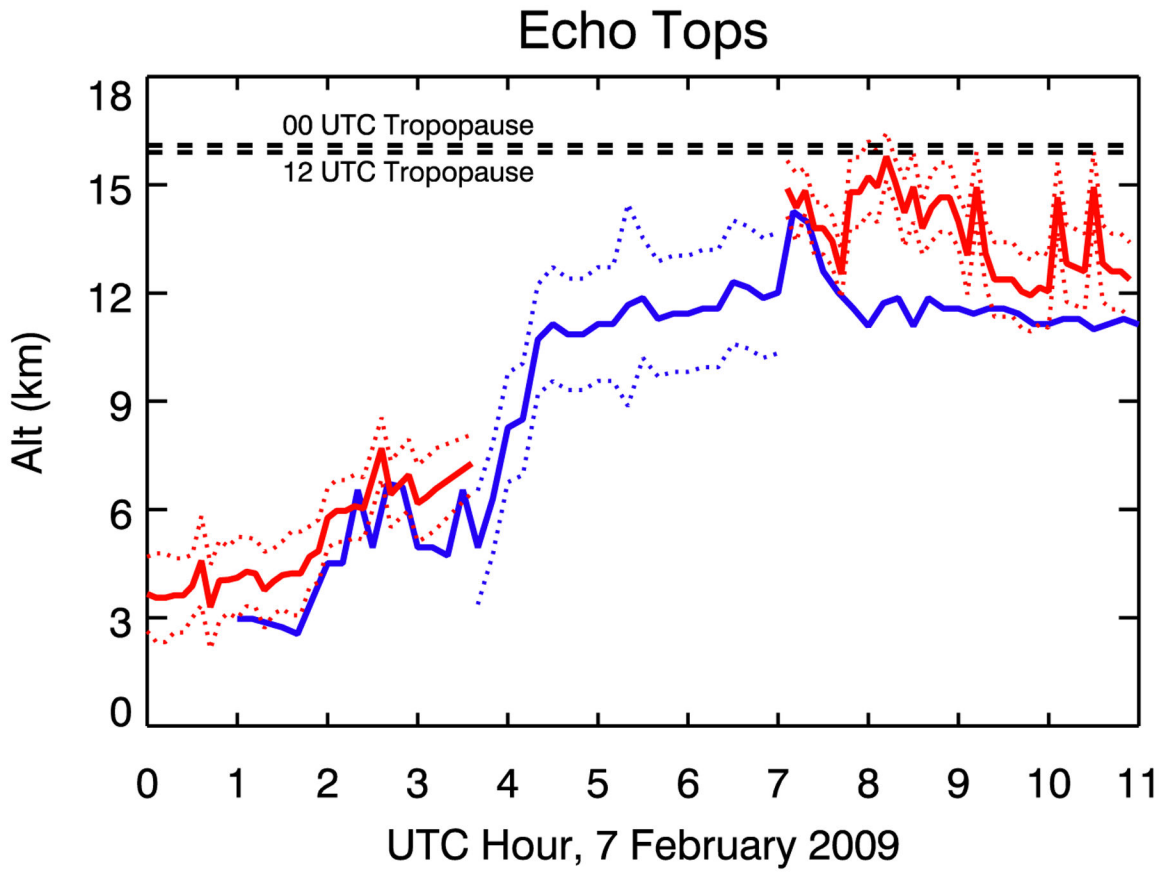

Figure 6.

Echo top heights from Laverton (red) and Yarrowonga (blue) radar stations near Melbourne. Solid lines represent the centroid of the echo-top pixel. Dotted lines are for the top and bottom of the echo-top pixel. Horizontal dashed lines are the tropopause heights calculated for Melbourne's location at 00 and 12 UTC. Data are from the Australian Bureau of Meteorology.

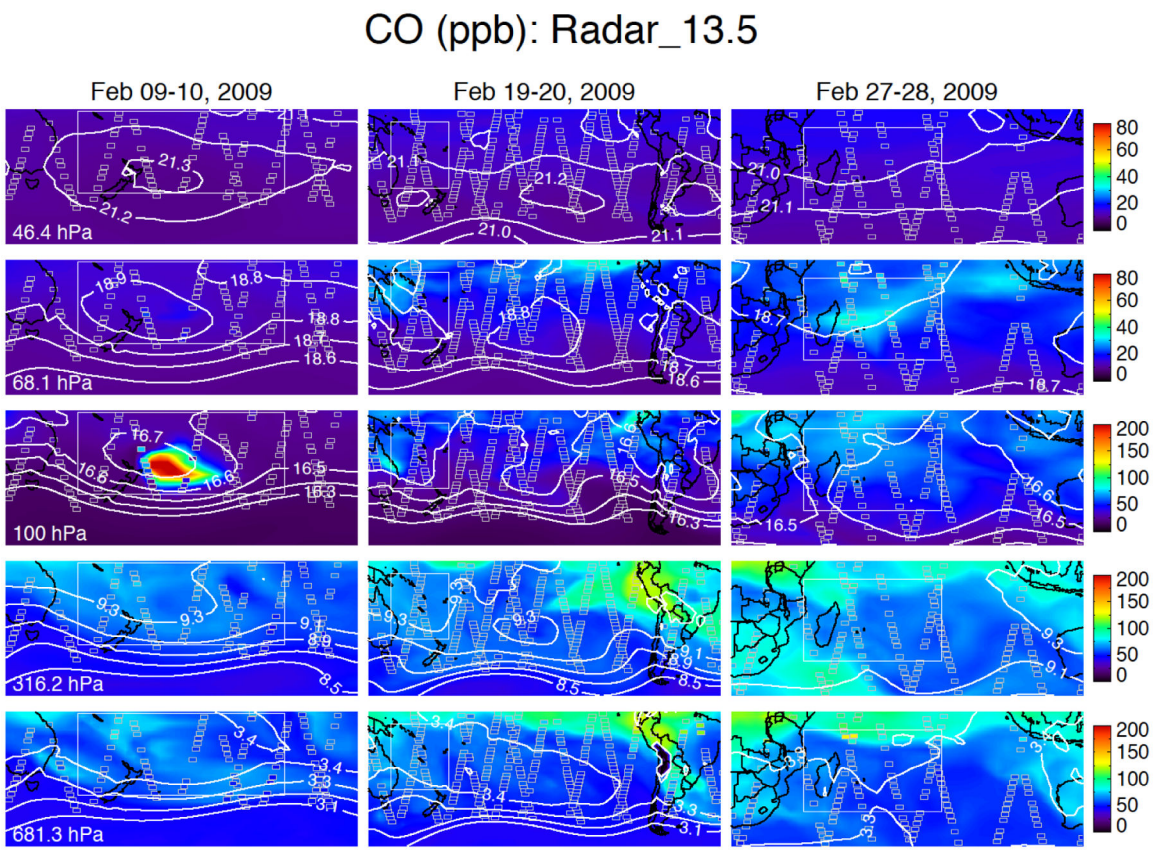

Figure 7.

Same as Figure 4, but for the 13.5 km injection height corresponding to radar estimates of injection height (Figure 6).

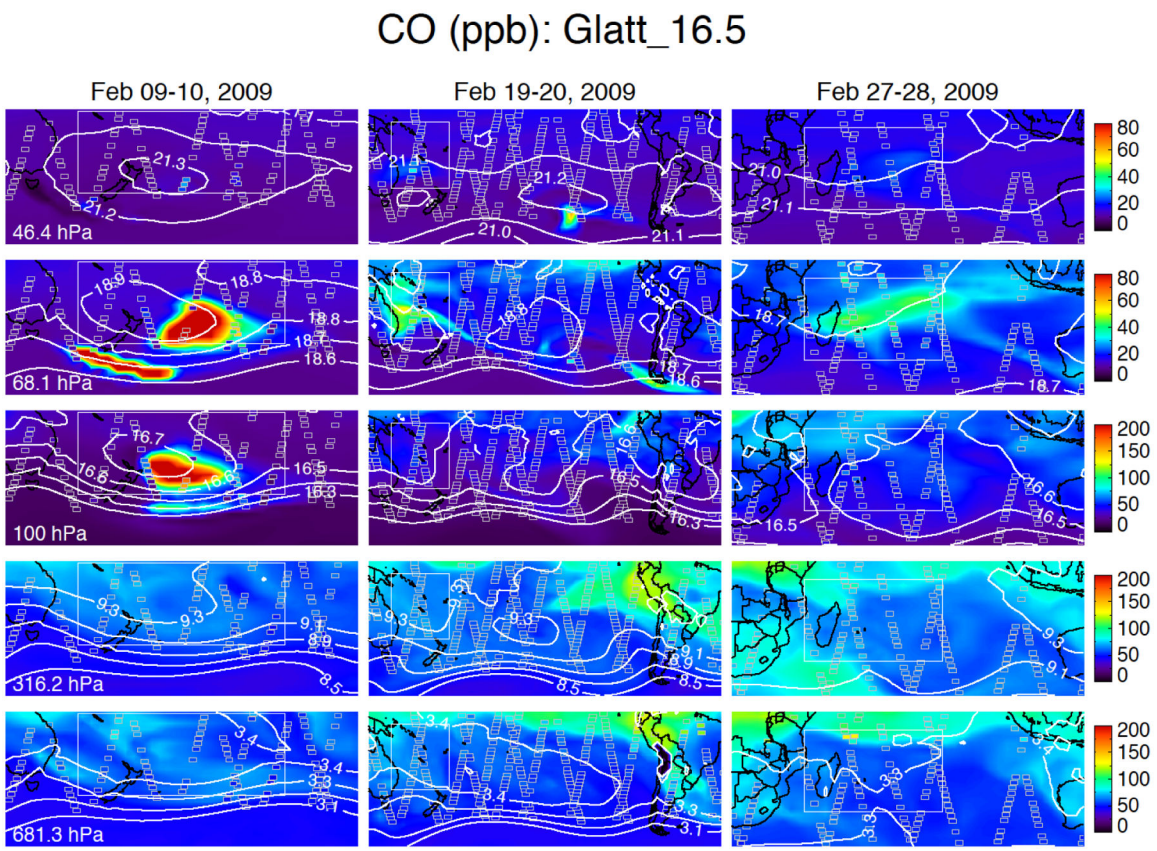

Figure 8.
Same as Figure 4, but for the 16.5 km injection height of Glatthor et al. [2013].

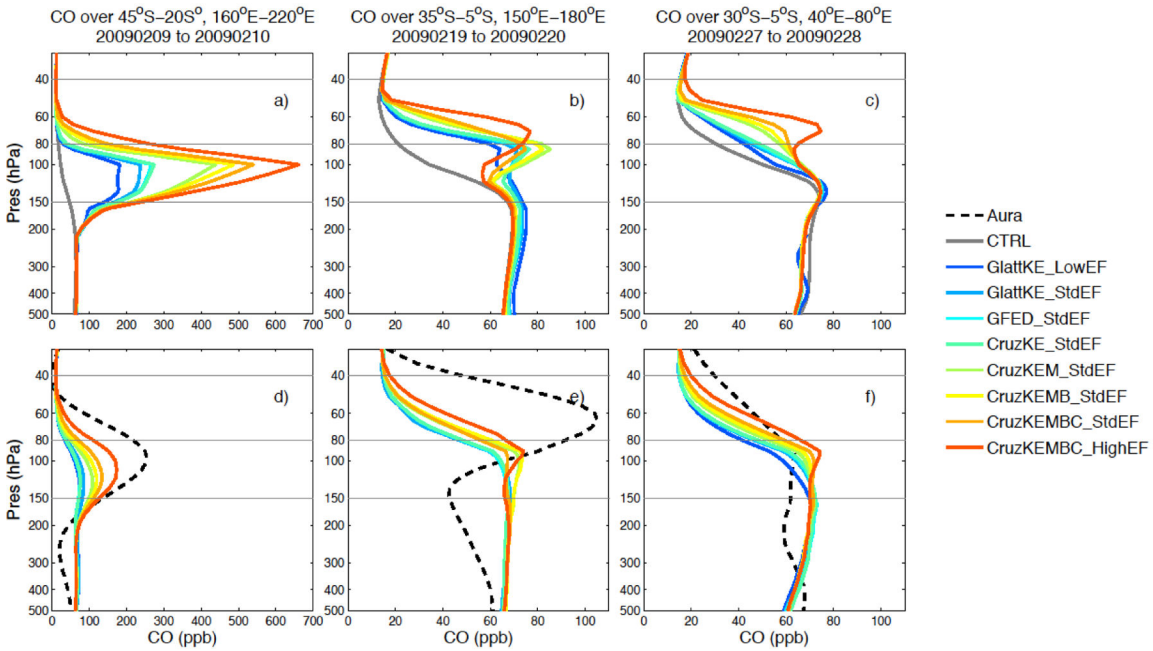

Figure 9.

Vertical CO profiles for different emissions amounts for a 13.5 km injection height, for profiles with CO thresholds greater than specified in text. NE of New Zealand on February 9/10 (left), over Coral Sea on February 19/20 (middle), east of Madagascar on February 27/28 (right). Top row shows raw model profiles, bottom row shows model profiles after averaging kernel smoothing. Horizontal lines show the layers in the upper troposphere / lower stratosphere (150 hPa to 80 hPa) and strictly the lower stratosphere (80 hPa to 40 hPa) over which CO is compared to emissions. Note change in CO scale on x-axis.

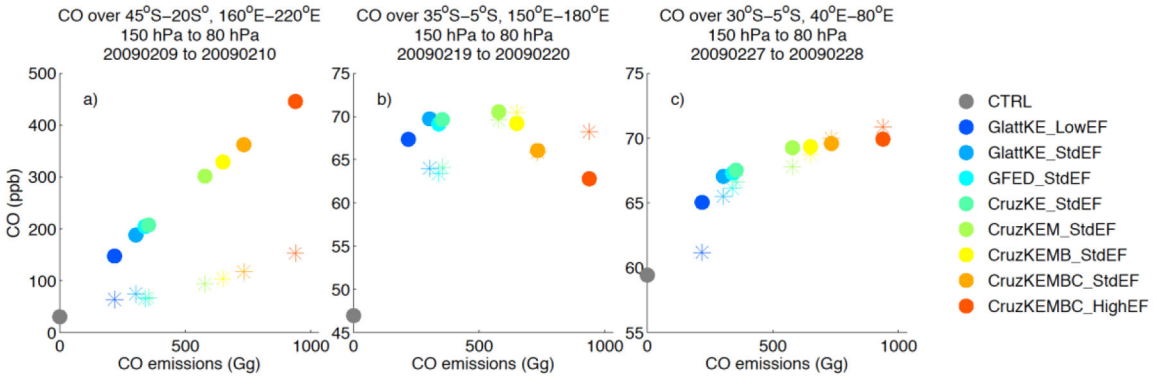

Figure 10.

CO in the UTLS (between 150 and 80 hPa) as a function of CO emissions on February 7 for a) NE of New Zealand on February 9/10, b) over the Coral Sea on February 19/20, and c) east of Madagascar on February 27/28 (right). Solid circles are the mean of all profiles exceeding height-specific CO thresholds for each region as in Figure 9 and defined in the text. Asterisks are the profiles exceeding the thresholds with Aura sampling and averaging kernel smoothing. Horizontal black line shows the Aura CO. Note changes in CO scale on y-axis. Atmospheric CO is plotted in terms of CO emissions, but BC, OC, NO_x and SO_2 emissions were increased concurrently.

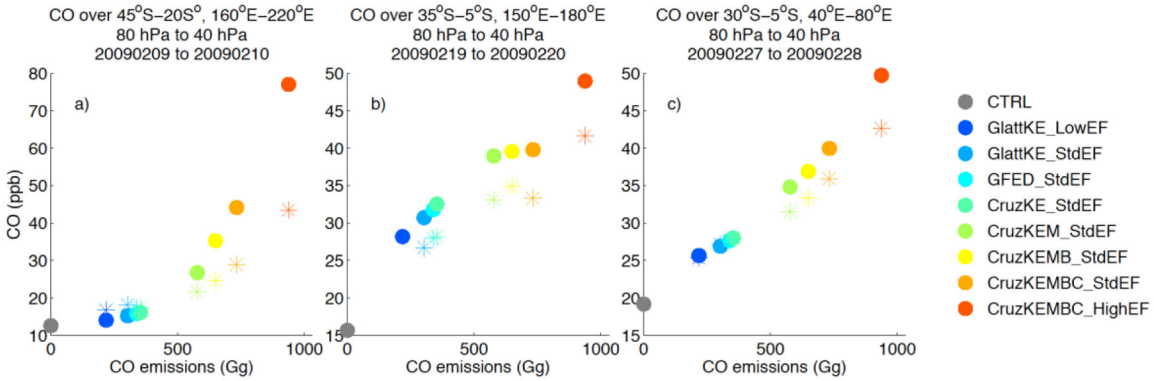

Figure 11.
Same as Figure 10 but for CO in the lower stratosphere (between 80 and 40 hPa).

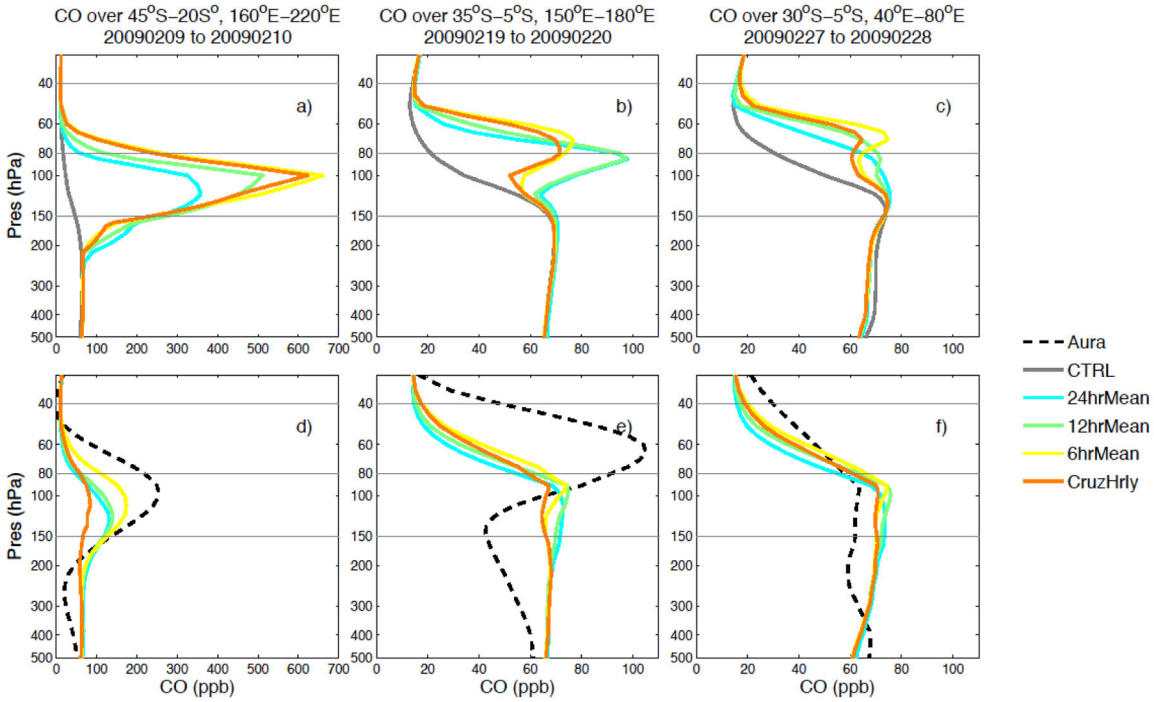

Figure 12.

Same as Figure 9, but for the high emissions amount (CruzKEMBC_HighEF) distributed according to different emissions timing scenarios.

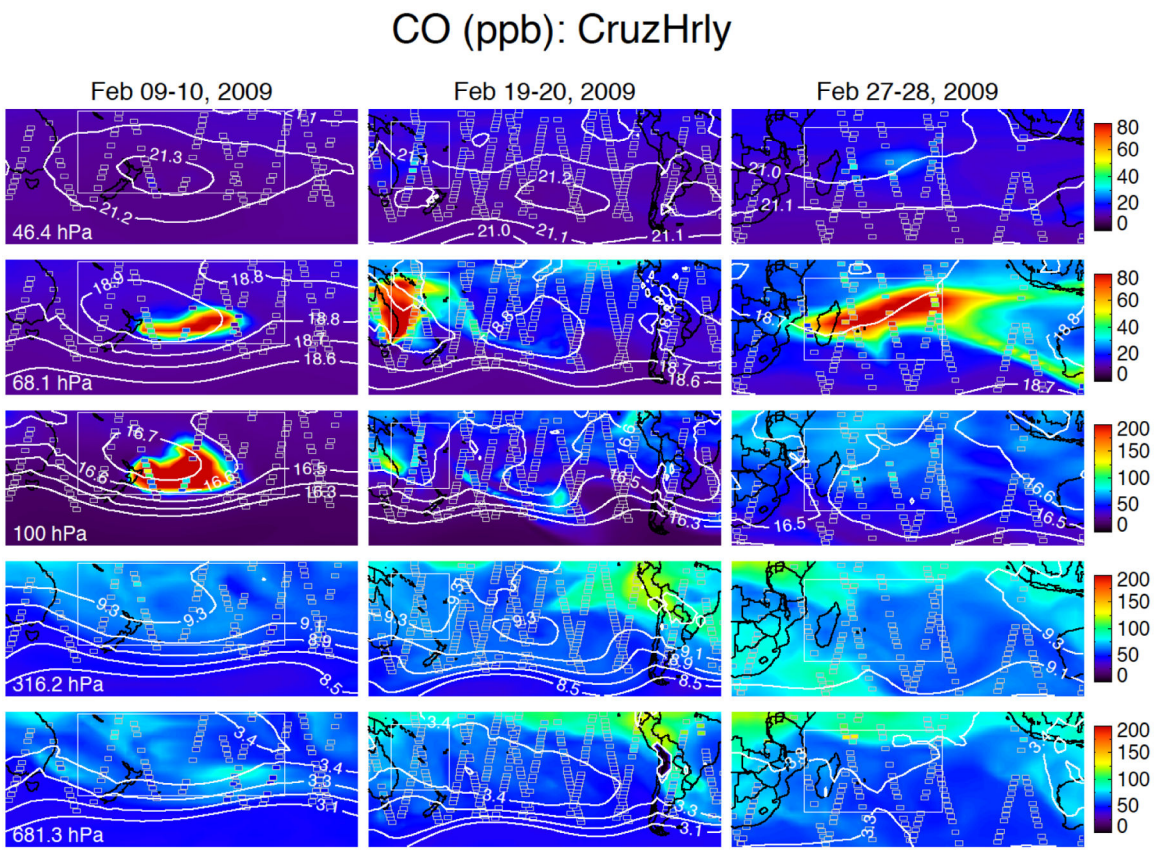

Figure 13.

Same as Figure 4, but for the 13.5 km injection height, highest emissions scenario, and burn period timing from Cruz et al. [2012].

Table 1.

Emissions scenarios for the Black Saturday fires on February 7, 2009. Scenarios are named according to, variously, the source of the injection height estimate, the emissions amount and the emissions timing. AM01 refers to Andreae and Merlet [*Andreae and Merlet*].

	Name	Description	Injection height	Fuel consumed (Tg)	AM01 Emissions factors	Emissions timing
	CTRL	No Black Saturday emissions	-	0	-	-
Injection height tests	deLaat_3.5	de Laat et al. [2012] 'Low layer' initialization	3.5 km +/− 2 model layers	2.8	Mid-range	6-hour pulse centered on 11 UTC February 7 2009
	deLaat_8.5	de Laat et al. [2012] 'High layer' initialization	8.5 km +/− 2 model layers	2.8	Mid-range	6-hour pulse centered on 11 UTC February 7 2009
	Radar_13.5	Cloud echo top estimates from radar	13.5 km +/− 2 model layers	2.8	Mid-range	6-hour pulse centered on 11 UTC February 7 2009
	Glatt_16.5	Glatthor et al. [2013] estimate for model without interactive aerosols	16.5 km +/− 2 model layers	2.8	Mid-range	6-hour pulse centered on 11 UTC February 7 2009
Emissions amount tests	Glatt_LowEF	Glatthor et al. [2013] fuel consumption, low AM01 emissions factors	13.5 km +/− 2 model layers	2.8	Low	6-hour pulse centered on 11 UTC February 7 2009
	GFED_StdEF	GFED fuel consumption, standard AM01 emissions factors	13.5 km +/− 2 model layers	3.2	Mid-range	6-hour pulse centered on 11 UTC February 7 2009
	CruzKE_StdEF	Cruz Kilmore East fuel consumption, standard AM01 emissions factors	13.5 km +/− 2 model layers	3.3	Mid-range	6-hour pulse centered on 11 UTC February 7 2009
	CruzKEM_StdEF	with Kilmore East, Murrindindi fire from Gellie	13.5 km +/− 2 model layers	5.4	Mid-range	6-hour pulse centered on 11 UTC February 7 2009
	CruzKEMB StdEF	with Kilmore East, Murrindindi, Bunyip fires from Gellie	13.5 km +/− 2 model layers	6.1	Mid-range	6-hour pulse centered on 11 UTC February 7 2009
	CruzKEMBC_StdEF	with Kilmore East, Murrindindi, Bunyip and Churchill fires from Gellie	13.5 km +/− 2 model layers	6.8	Mid-range	6-hour pulse centered on 11 UTC February 7 2009
	CruzKEMBC_HighEF	with Kilmore East, Murrindindi, Bunyip and Churchill fires, high AM01 emissions factors	13.5 km +/− 2 model layers	6.8	High	6-hour pulse centered on 11 UTC February 7 2009
Emissions timing tests	24hrMean	Daily mean emissions	13.5 km +/− 2 model layers	6.8	High	Uniform hourly release over 24- hours corresponding to GFED resolution
	12hrMean	12 hour emissions	13.5 km +/− 2 model layers	6.8	High	Uniform hourly release over 12- hours

	Name	Description	Injection height	Fuel consumed (Tg)	AM01 Emissions factors	Emissions timing
	CruzHrly	Hourly emissions	13.5 km +/− 2 model layers for peak burning period, 3.5 km otherwise	6.8	High	Varying hourly according to Cruz burn period energy output

Table 2.

Emissions factor ranges (g/kg) from Andreae and Merlet [2001]. No uncertainty estimate is provided for SO_2.

Species	Low	Mid-range	High
CO	77	107.0	137.0
NO_X	1.6	3.0	4.4
SO_2	1.0	1.0	1.0
BC	0.37	0.56	0.75
OC	8.6	9.15	9.7